

# EFFECT OF ACCRETING TIDALLY DISRUPTED STARS ON THE SPIN EVOLUTION OF $\sim 10^6 M_\odot$ BLACK HOLES

XIAOXIA ZHANG<sup>1,2,3</sup>, YOUJUN LU<sup>1,2,4†</sup>, AND ZHU LIU<sup>1</sup>

<sup>1</sup> National Astronomical Observatories, Chinese Academy of Sciences, Beijing 100012, China; †luyj@nao.cas.cn

<sup>2</sup> School of Astronomy and Space Sciences, University of Chinese Academy of Sciences, No. 19A Yuquan Road, Beijing 100049, China

<sup>3</sup> Department of Astronomy, Xiamen University, Xiamen, Fujian, 361005, China

<sup>4</sup> CAS Key laboratory for computational Astrophysics, National Astronomical Observatories, Chinese Academy of Sciences, Beijing, 100012, China

*Draft version May 14, 2019*

## ABSTRACT

Accretion of tidally disrupted stars (TDSs) is expected to contribute significantly to the growth of massive black holes (MBHs) with mass  $\sim 10^6 M_\odot$  in galactic centers. In this paper, we quantitatively investigate the effect of the TDS accretion on the spin evolution of these relatively small MBHs, by also considering the accretion of gas-clouds with (many) chaotic episodes. We find that the accretion of TDSs can play an important role or even a dominant role in shaping the spin distribution of  $\sim 10^6 M_\odot$  MBHs, depending on the contribution fraction ( $f_{\text{TDE}}$ ) of the TDS accretion to the MBH growth. If  $f_{\text{TDE}}$  is as large as  $\gtrsim 0.9$ , most  $\sim 10^6 M_\odot$  MBHs have low spins ( $|a| \lesssim 0.3$ ); if  $f_{\text{TDE}}$  is as small as  $\lesssim 0.1$ , most  $\sim 10^6 M_\odot$  MBHs have high spins ( $|a| \gtrsim 0.7$ ). We also find that (1) the fraction of highly spinning  $\sim 10^6 M_\odot$  MBHs in the TDS accretion states is smaller than that in the gas-cloud (AGN) accretion states, which is a consequence of more rapid spin decrease during the period of consecutive TDS accretion than the spin increase during the AGN periods when the spin is large; (2) the fraction of retrograde spin accretion in the TDS accretion states is almost the same as that of prograde spin accretion, while it is negligible in the gas-cloud (AGN) accretion states. Current scarce sample of AGNs ( $\sim 10^6 M_\odot$ ) with spin measurements hints an insignificant contribution from TDS accretion to MBH growth. Future measurements on spins of  $\sim 10^6 M_\odot$  MBHs may provide stronger constraints on the importance of both AGN and TDS accretion states in their growth history.

*Subject headings:* accretion, accretion disks; black hole physics; galaxies: active; galaxies: nuclei; relativistic processes

## 1. INTRODUCTION

Massive black holes (MBHs) exist almost ubiquitously in galactic centers (e.g., Kormendy & Ho 2013), which are believed to be fully specified by their masses and spins (Kerr 1963). It has been demonstrated that the spin distribution of MBHs may contain important information about the MBH formation and assembly history and thus may be used to put constraints on their growth history (e.g., Volonteri et al. 2005; King & Pringle 2006; Volonteri et al. 2007; Berti & Volonteri 2008; King et al. 2008; Perego et al. 2009; Sądowski et al. 2011; Volonteri et al. 2013; Dotti et al. 2013; Sesana et al. 2014), in addition to the mass distribution and the AGN luminosity function (e.g., Sołtan 1982; Yu & Tremaine 2002; Marconi et al. 2004; Yu & Lu 2004, 2008; Shankar et al. 2009).

The accretion modes that MBHs experienced play a leading role in determining the MBH spin evolution (e.g., Volonteri et al. 2007). Coherent accretion, whether via thick disk or the standard thin disk, leads to rapid spin-up of the central MBH, while “chaotic” accretion, composed of many episodes with randomly distributed disk orientations, may lead to spin-down of a rapidly rotating MBH. Therefore, the spins of most active MBHs should be close to 1 if their growth is dominated by coherent accretion, and they may be close to 0 if their growth is dominated by chaotic accretion with sufficiently small disk mass in each accretion episode.

Currently there are more than two dozen MBHs in AGNs having spin estimations, mainly by using the profile of Fe  $K\alpha$  line and the X-ray reflection spectroscopy, and most of those MBHs are rapidly rotating with spin  $\gtrsim 0.8$  (e.g., Brenneman & Reynolds 2006; Brenneman 2013; Reynolds 2014; Vasudevan et al. 2016). High radiative efficiencies inferred for some QSOs also suggest rapidly spinning MBHs in those QSOs (e.g., Trakhtenbrot 2014; Capellupo et al. 2016). However, Liu et al. (2015) recently showed that those MBHs in narrow-line Seyfert 1s (NLS1s), typically with mass  $\sim 10^6 M_\odot$ , may not be spinning very fast in general according to the profile of the broad relativistic Fe  $K\alpha$  line found in the stacked spectrum of a large number of NLS1s. It is not clear whether the apparently low spins of those MBHs in NLS1s are due to their different growth histories.

Tidal disruption of stars was first predicted as an exotic phenomenon inevitably resulting from the existence of MBHs in the centers of galaxies (e.g., Hills 1975; Rees 1988), and later confirmed by observations (e.g., as summarized in Komossa 2015). The predicted rate of TDEs is about  $10^{-4} - 10^{-3} \text{ yr}^{-1}$  for small galaxies with  $\sim 10^6 M_\odot$  MBHs and  $10^{-6} - 10^{-5} \text{ yr}^{-1}$  for big galaxies with  $\gtrsim 10^7 M_\odot$  MBHs (e.g., Magorrian & Tremaine 1999; Wang & Merritt 2004; Kesden 2012). By using TDEs found in various surveys, such as the ROSAT all-sky survey, the XMM-Newton slew survey, the Galaxy Evolution Explorer (GALEX) survey, and the Sloan Dig-

ital Sky Survey (SDSS), the TDE rate has also been frequently estimated and the value is generally  $\sim 10^{-5} \text{ yr}^{-1}$  per galaxy (e.g., Donley et al. 2002; Esquej et al. 2008; Gezari et al. 2008; van Velzen & Farrar 2014). The discrepancy between the theoretical and observational rates could be caused by various factors such as selection effect, small number statistics, and dust extinction (see Stone & Metzger 2016). If small galaxies do have a higher TDE rate as suggested by theoretical studies (e.g., Wang & Merritt 2004), the accretion of TDSs over the cosmic time would dominate or contribute significantly to the mass growth of  $\sim 10^6 M_\odot$  MBHs (see, e.g., Milosavljević et al. 2006), though it contributes little to the growth of  $\gtrsim 10^7 M_\odot$  MBHs as the TDE rate for those MBHs is much smaller.

Accretion of TDSs may also affect the spin evolution of MBHs, especially the small ones with mass  $\sim 10^6 M_\odot$ , in addition to the AGN accretion modes mentioned above. Volonteri et al. (2007) have pointed out that the significance of accreting TDSs in the growth histories of  $\sim 10^6 M_\odot$  MBHs may lead to the spin distribution of those MBHs significantly different from that for MBHs with mass substantially larger than  $10^7 M_\odot$ . In this paper, we quantitatively investigate the effect of accreting TDSs on the spin evolution of  $\sim 10^6 M_\odot$  MBHs, whether this effect could lead to a spin distribution of those AGNs with  $\sim 10^6 M_\odot$  MBHs significantly different from that of  $> 10^7 M_\odot$  MBHs, and whether it can be used to constrain the significance of TDS accretion to the growth of those MBHs.

This paper is organized as follows. In Section 2, we consider an evolution model for MBHs with mass  $\sim 10^6 M_\odot$ <sup>1</sup>, which grow up via the accretion of numerous tidally disrupted stars (TDSs) and a number of gas-clouds on orbits with random orientations relative to the MBH equatorial plane. More detailed physics about the TDS and gas-cloud accretion are considered here compared with previous analytic studies on TDS effect on MBH spin evolution in Volonteri et al. (2005) and chaotic gas-cloud accretion in King et al. (2008). Our results on the spin distribution of MBHs in both the gas-cloud (AGN) accretion episodes and the TDS accretion episodes obtained from some example models are presented in Section 3. According to those results, we obtain some implications on the importance of the TDS accretion to the growth of  $\sim 10^6 M_\odot$  MBHs from current spin measurements in Section 4. Conclusions and discussions are given in Section 5.

## 2. SPIN EVOLUTION OF $\sim 10^6 M_\odot$ MBHs

To investigate the effect of accreting TDSs on the spin evolution of  $\sim 10^6 M_\odot$  MBHs, we assume an initial mass of  $10^5 M_\odot$  and a final masses of  $10^{6.5} M_\odot$  for those MBHs<sup>2</sup>, and they grow up by accreting (1) TDSs

<sup>1</sup> The effect of mergers is not considered in this paper as those  $\sim 10^6 M_\odot$  MBHs, mainly in the bulges of spiral galaxies, probably did not experience a significant number of major mergers in their assembly histories.

<sup>2</sup> We simply choose such a mass range as our goal in the present paper is to investigate how accretion of TDSs influences the spin evolution of  $\sim 10^6 M_\odot$  MBHs. Adopting a smaller initial MBH mass does not affect our results; adopting a substantially larger final MBH mass ( $> 10^7 M_\odot$ ) does affect our results, but we have argued that the contribution from TDS accretion to those is in-

and (2) giant gas-clouds falling in. Since the plug-in orbits of TDSs or the infalling gas-cloud may be randomly oriented, the accretion disks can be either on the MBH equatorial plane or inclined to it. Therefore, the mass growth and spin evolution of the MBH are generally controlled by the amount of material falling into the MBH from the inner disk boundary and the torque exerted by the (inclined) disk on the MBH spin. In general, the MBH mass growth rate is determined by (e.g., see Thorne 1974)

$$\frac{dM_\bullet}{dt} = f_{\text{Edd}} \frac{E_{\text{in}}}{1 - E_{\text{in}}} \frac{M_\bullet}{t_{\text{Edd}}}, \quad (1)$$

where  $f_{\text{Edd}}$  is the Eddington ratio,  $E_{\text{in}}$  is the specific energy of the accreted material at the disk inner boundary  $r_{\text{in}}$  which may be coincident with the innermost stable circular orbit (ISCO), and  $t_{\text{Edd}} = 4.5 \times 10^8 \text{ yr}$  is the Eddington timescale. The MBH angular momentum ( $\mathbf{J}_\bullet$ ) evolution is controlled by

$$\frac{d\mathbf{J}_\bullet}{dt} = \dot{M} r_g c L_{\text{in}} \hat{\mathbf{l}} + \frac{4\pi G}{c^2} \int_{\text{disk}} \frac{\mathbf{L} \times \mathbf{J}_\bullet}{r^2 \cdot r_g} dr, \quad (2)$$

where  $\dot{M}$  is the accretion rate at  $r_{\text{in}}$ ,  $L_{\text{in}}$  is the specific angular momentum at  $r_{\text{in}}$ ,  $\mathbf{L}$  is the angular momentum vector of disk per unit area,  $\hat{\mathbf{l}}$  is a unit vector parallel to  $\mathbf{L}(r_{\text{in}})$ , and  $r$  is in unit of gravitational radius  $r_g (= GM_\bullet/c^2$  with  $G$  the gravitational constant and  $c$  the speed of light; see also Perego et al. 2009; Dotti et al. 2013 for Eq. (2)). The first term at the r.h.s. of Equation (2) represents the contribution from the angular momentum brought in by material falling from the disk inner boundary, and the second term at the r.h.s. of Equation (2) represents the coupling between the MBH spin and the disk angular momentum i.e., the Lense-Thirring (LT) precession (Lense & Thirring 1918). This leads to a warped accretion disk, with the inner region bent to the MBH equatorial plane and the outer region keeping the original misalignment (Bardeen & Petterson 1975), and may further lead to a gradual alignment (or anti-alignment) of the MBH and disk angular momenta. If the initial angle  $\beta$  between  $\mathbf{J}_{\text{disk}}$  and  $\mathbf{J}_\bullet$  satisfies the condition  $\cos \beta < -J_{\text{disk}}/2J_\bullet$ , then the system will finally reach a stable counter-alignment configuration, and otherwise the alignment will be the case (King et al. 2005).

If the disk is on the equatorial plane of the MBH, then the second term vanishes, and combining Equations (1), Equations (2) is reduced to (e.g., Thorne 1974; Barausse 2012; Dotti et al. 2013)

$$\frac{da}{dt} = (L_{\text{in}} - 2aE_{\text{in}}) \frac{f_{\text{Edd}}}{(1 - E_{\text{in}})t_{\text{Edd}}}, \quad (3)$$

where  $E_{\text{in}}$  and  $L_{\text{in}}$  are values at ISCO of equatorial disk, and  $a$  is the dimensionless spin parameter with  $|a| = \frac{c|\mathbf{J}_\bullet|}{GM_\bullet^2}$ . Throughout this paper,  $a$  is positive if the disk is co-rotating around the MBH, and negative if counter-rotating around the MBH.

In this paper, we consider the accretion of TDSs and gas-clouds separately and ignore the possibility of accreting TDSs during the gas-cloud (AGN) accretion episodes. The main reasons are as follows. First, if a

significant.

star is tidally disrupted during a gas-cloud (AGN) accretion episode, the star before its disruption or the tidal debris after the disruption may ground down quickly due to its interaction with the accretion disk and become part of the disk (cf., Artymowicz et al. 1993; Miralda-Escudé & Kollmeier 2005). Second, currently it is still not clear what exactly the signal is from a TDE occurred in the gas-cloud (AGN) accretion episodes and it is difficult to identify such an event (but Blanchard et al. 2017). Third, the AGN lifetime is short compared with the cosmic time, and thus the contribution of those TDSs to the MBH mass growth and spin evolution during the gas-cloud (AGN) accretion episode(s) is insignificant, provided a more or less constant TDE rate for any individual galaxies. Note also that we only consider the spin evolution of MBHs due to accretion of TDSs and gas-clouds, and ignore the effect of any other processes and the intervals between any two adjacent accretion episodes. With such a setting, the MBH may be detected as a ‘TDE’ when it accretes through the TDS channel, or as a normal ‘AGN’, possibly an NLS1, when it accretes via the standard thin disk at a rate close to the Eddington limit through the gas-cloud accretion channel.

### 2.1. Accretion of tidally disrupted stars

Normally a TDE occurs when a star moves so close to an MBH that the periapsis of its orbit  $r_p$  is less than the tidal radius

$$r_{\text{tid}} = D_* \left( \frac{M_\bullet}{M_*} \right)^{1/3} = 0.47 \text{ AU } x_* \left( \frac{M_{\bullet,6}}{m_*} \right)^{1/3}, \quad (4)$$

where  $D_*$  and  $M_*$  are the radius and mass of the star, respectively,  $x_*$  is the radius of the star in unit of the solar radius,  $M_{\bullet,6}$  is the MBH mass in unit of  $10^6 M_\odot$ , and  $m_*$  is the stellar mass in unit of  $M_\odot$ . For simplicity, in this paper we assume that the TDSs all have the solar mass and the solar radius, i.e.,  $x_* = 1$  and  $m_* = 1$ . Assuming a mass spectrum for TDSs introduces little effect to our results presented in Section 3.

Once a star is tidally disrupted, roughly half of its mass is ejected, and the other half is bound to the MBH. The debris of the bound part starts to fall back to their pericenter after a time  $t_{\text{min}} \sim 41 M_{\bullet,6}^{1/2}$  day with a rate of

$$\dot{M}_{\text{fb}} = \dot{M}_p \left( \frac{t}{t_{\text{min}}} \right)^{-5/3}, \quad (5)$$

where  $\dot{M}_p = M_\odot / 3t_{\text{min}} \sim 1.9 \times 10^{26} M_{\bullet,6}^{-1/2} \text{ g s}^{-1}$  is the peak of the fallback rate (e.g., Lodato & Rossi 2011). The fallback rate is larger than the Eddington limit  $\dot{M}_{\text{Edd}} \simeq L_{\text{Edd}} / \eta c^2 = 1.4 \times 10^{24} M_{\bullet,6} (\eta / 0.1)^{-1} \text{ g s}^{-1}$  at the beginning if  $M_{\bullet,6} \lesssim 25$ , where  $\eta$  is the radiative efficiency of the MBH, and  $L_{\text{Edd}} = 1.3 \times 10^{44} M_{\bullet,6} \text{ erg s}^{-1}$  is the Eddington luminosity. Therefore, the accretion of the debris of a TDS can be divided into two stages: an initial stage with  $\dot{M}_{\text{fb}} > \dot{M}_{\text{Edd}}$ , in which the accretion may be via thick disk with outflows, and a second stage with  $\dot{M}_{\text{fb}} < \dot{M}_{\text{Edd}}$ , in which the accretion may be via the standard thin disk.

It has been suggested that most of the debris may be expelled via outflows and the actual rate at the inner edge

$r_{\text{in}}$  of the disk is at most about the Eddington value, although the accretion rate exceeds the Eddington limit in the first stage (e.g., Franchini et al. 2016). Therefore, we assume that the factor  $f_{\text{Edd}}$  in the r.h.s. of Equation (1) is equal to  $\min(\dot{M}_{\text{fb}} / \dot{M}_{\text{Edd}}, 1)$  for the TDS accretion.

The disk formed by TDS debris may not be on the equatorial plane of the MBH initially since the stellar orbits of TDSs are probably isotropically distributed, as suggested by studies of loss cone stars surrounding massive binary black holes, in which those stars are found to be on chaotic orbits with random orientations (see Cui & Yu 2014; Vasiliev et al. 2015). On the one hand, the inner disk may also not be on the equatorial plane for this inclined TDS disk configuration (see Section 2.1.2). The specific energy ( $E_{\text{in}}$ ) and angular momentum ( $L_{\text{in}}$ ) at the inner disk boundary (presumably the ISCO) have already been given in the literature for equatorial disks (e.g., Bardeen et al. 1972). However, those quantities for inclined disks are different from the equatorial case and are not explicitly given in the literature. Therefore, it is necessary to calculate  $E_{\text{in}}$  and  $L_{\text{in}}$  for disks with different inclination angles at the inner edge in order to solve Equations (1) and (2) that govern the MBH mass and spin evolution. On the other hand, the misalignment between the angular momenta of the disk and MBH leads to the generation of torques on both the disk and MBH (the second term at the r.h.s. of Eq. 2) and thus the precession and eventual alignment of them. Below we first introduce the procedures to calculate  $r_{\text{in}}$ ,  $E_{\text{in}}$ , and  $L_{\text{in}}$  for an inclined disk in Section 2.1.1, then describe the precession and alignment of the TDS disk due to the disk angular momentum-MBH spin coupling in Section 2.1.2, and finally present the method to solve the mass and spin evolution equations in Section 2.1.3.

#### 2.1.1. Specific energy and angular momentum at the inner boundary of an inclined disk

We adopt the Boyer-Lindquist coordinate system ( $t, r, \theta', \phi'$ ) to describe the MBH metric. For an MBH with any given spin  $a$  and a non-equatorial disk with any inclination angle  $i$ ,<sup>3</sup>  $r_{\text{in}}$ ,  $E_{\text{in}}$  and  $L_{\text{in}}$  can be calculated by the following procedures. Note that similar method was adopted by Hughes (2000, 2001, see also Stone et al. 2013) to calculate the properties of non-equatorial circular orbits around Kerr black holes.

First, we calculate the ISCO (in unit of  $r_g$ ) for an equatorial disk according to (Bardeen et al. 1972)

$$r_{\text{ISCO}} = 3 + Z_2 \mp [(3 - Z_1)(3 + Z_1 + 2Z_2)]^{1/2}, \quad (6)$$

where  $Z_1 = 1 + (1 - a^2)^{1/3} [(1 + a)^{1/3} + (1 - a)^{1/3}]$ ,  $Z_2 = (3a^2 + Z_1^2)^{1/2}$ , and the upper/lower case of the “ $\mp$ ” (or “ $\pm$ ”) signs represents for prograde/retrograde orbits (the same afterwards). The specific energy  $E_{\text{ISCO}}$  and angular momentum  $L_{\text{ISCO}}$  at  $r_{\text{ISCO}}$  are then calculated through

$$E(r) = \frac{r^{3/2} - 2r^{1/2} + a}{r^{3/4}(r^{3/2} - 3r^{1/2} + 2a)^{1/2}}, \quad (7)$$

$$L(r) = \pm \frac{r^2 - 2ar^{1/2} + a^2}{r^{3/4}(r^{3/2} - 3r^{1/2} + 2a)^{1/2}}, \quad (8)$$

<sup>3</sup> Here  $i$  is defined as the angle between the orbital angular momentum of the disk at the inner edge and the MBH spin vector, and hence  $i = 0, \pi/2$ , and  $\pi$  correspond to the prograde equatorial orbit, polar orbit, and retrograde equatorial orbit, respectively.

by setting  $r = r_{\text{ISCO}}$ .

Second, fix  $r = r_{\text{ISCO}}$  for prograde orbits, decrease the energy  $E$  from the starting point  $E_{\text{ISCO}}$ , and calculate the  $z$ -direction angular momentum  $L_z$  and the Carter constant  $Q$  via

$$L_z(r, E) = \frac{E(r^2 - a^2) - \Delta \sqrt{r^2(E^2 - 1) + r}}{a(r - 1)}, \quad (9)$$

$$Q(r, E) = \frac{[(a^2 + r^2)E - |a|L_z(r, E)]}{\Delta} - B, \quad (10)$$

where  $\Delta = r^2 - 2r + a^2$  and  $B \equiv r^2 + a^2 E^2 - 2|a|EL_z(r, E) + L_z(r, E)^2$  (see Hughes 2000, 2001). We further check whether  $d^2R/dr^2$  equals zero; if not, then increase  $r$  to repeat the above procedures until reaching  $d^2R/dr^2 = 0$ , the condition for the innermost circular orbit, or until an unphysical  $L_z$  or  $Q$  is reached. Here  $R$  is defined as  $R \equiv [E(r^2 + a^2) - |a|L_z]^2 - \Delta [r^2 + (L_z - |a|E)^2 + Q]$ , and the orbital motion equations are  $\Sigma^2(d\tau/dr)^2 = R$ ,  $\Sigma^2(d\theta/d\tau)^2 = Q - \cot^2 \theta' L_z^2 - a^2 \cos^2 \theta' (1 - E^2)$ , and  $\Sigma(d\phi/d\tau) = \csc^2 \theta' L_z + |a|E[(r^2 + a^2)/\Delta - 1] - a^2 L_z/\Delta$ , with  $\Sigma \equiv r^2 + a^2 \cos^2 \theta'$ . If  $d^2R/dr^2 = 0$ , then we record  $r$ ,  $E$ ,  $Q$ ,  $L_z$ , and the inclination angle  $i$ .

The total angular momentum for a non-equatorial plane circular orbit is not conserved because of the LT and frame-dragging effects. For example, the LT effect causes the orbit to precess around, i.e.,  $\theta'$  is not a constant. For non-equatorial circular orbits, it can be described as  $L_{\text{tot}}^2(\theta') = Q + L_z^2 - a^2 \cos^2 \theta' (1 - E^2)$  (e.g., de Felice 1980; Frolov & Novikov 1998). Given a non-equatorial circular orbit with  $r_{\text{in}}$ ,  $E$ ,  $L_z$ , and  $Q$ , we estimate the maximum and minimum values of  $\theta'$ , i.e.,  $\theta'_{\text{max}}$  and  $\theta'_{\text{min}}$ , by solving the motion equation  $\Sigma d\theta'/d\tau = 0$ . Then we take  $\langle L_{\text{tot}} \rangle = [L_{\text{tot}}(\theta'_{\text{max}}) + 2L_{\text{tot}}(\pi/2) + L_{\text{tot}}(\theta'_{\text{min}})]/4$  as the mean specific angular momentum carried by the accreted material falling into the MBH from a circular orbit with  $r_{\text{in}}$ ,  $E_{\text{in}}$ ,  $L_z$ , and  $Q$ , which is also recorded for each non-equatorial circular orbit obtained above.

Third, decrease  $E$  again, and repeat the above procedures until  $r = r_{\text{ISCO}}$  for retrograde orbits. Hence an array of  $r_{\text{in}}$ ,  $E_{\text{in}}$ ,  $\langle L_{\text{tot}} \rangle$ ,  $L_z$ , and  $i$  is obtained for the innermost equatorial and non-equatorial circular orbits around an MBH with any given spin  $a$ .

Finally, for a disk with any given inclination angle  $i$ ,  $r_{\text{in}}$ ,  $E_{\text{in}}$  and  $L_{\text{in}}$  ( $\simeq \langle L_{\text{tot}} \rangle$ ) can be estimated by interpolation according to the array obtained above. Note here  $\eta = 1 - E_{\text{in}}$ .

Figure 1 shows the radius of the ISCO  $r_{\text{in}}$ , the specific energy and angular momentum at  $r_{\text{in}}$  as a function of the inclination angle of the orbit for an MBH with  $|a| = 0.1, 0.5, \text{ and } 0.9$ , respectively. As seen from Figure 1,  $r_{\text{in}}$  decreases with increasing  $\cos i$  and is in between that for retrograde ( $i = 180^\circ$ ) and prograde ( $i = 0^\circ$ ) orbits on the equatorial plane. The variation trends of  $E_{\text{in}}$  and  $L_{\text{in}}$  with the inclination angle are similar to that for  $r_{\text{in}}$ .

### 2.1.2. Disk angular momentum-MBH spin coupling: precession and alignment

We introduce two Cartesian reference frames here, in order to study the precession and alignment of the disk.

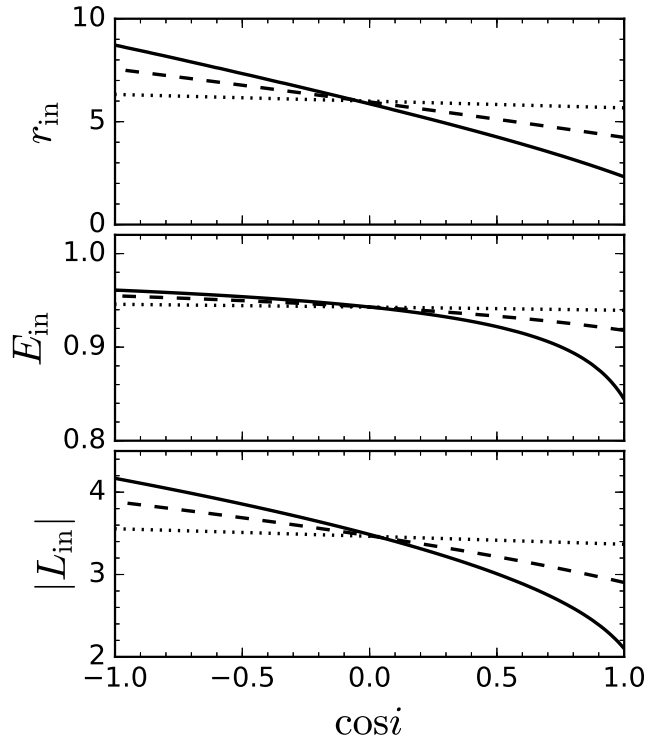


FIG. 1.— The radius of the innermost circular orbit  $r_{\text{in}}$  (top panel), the specific energy ( $E_{\text{in}}$ ; middle panel) and the specific angular momentum ( $L_{\text{in}}$ ; bottom panel) at  $r_{\text{in}}$ , as a function of the inclination angle  $i$  for both equatorial and non-equatorial orbits. Solid, dashed and dotted lines represent for  $|a|=0.9, 0.5$  and  $0.1$ , respectively. According to our definitions,  $\cos i = -1$  corresponds to retrograde equatorial disks, and  $\cos i = 1$  to prograde ones (see the footnote in Section 2.1.1).

One is the observer's rest frame  $Oxyz$  centered on the MBH, and the other is the rotating coordinate  $Ox'y'z'$  centered on the MBH and the  $z'$ -axis is always parallel with the MBH spin. Both of the Cartesian coordinates can be converted to spherical coordinates in terms of radius  $r$ , polar angle  $\theta$  and azimuthal angle  $\phi$ . In this subsection, quantities (vectors and angles) with superscript ' $'$ ' are in the  $Ox'y'z'$  frame. We assume that the initial direction of  $\mathbf{J}_{\text{disk}}$  for each TDS relative to the  $Oxyz$  frame is randomly oriented, i.e., the distribution for the azimuthal angle  $\phi$  is flat over  $0$  to  $2\pi$ , and the distribution for the polar angle  $\theta$  is proportional to  $\sin \theta$  over  $0$  to  $\pi$ .

The gravito-magnetic interaction between the MBH and an inclined TDS disk, at least at the initial super-Eddington accretion stage, will cause the precession and gradual alignment of their angular momenta, as detailed below.

(i) **Global precession:** The angular momentum of the disk per unit area in the  $Ox'y'z'$  reference frame can be expressed as

$$\mathbf{L}'(r) = \Sigma \Omega r^2 r_g^2 \hat{\lambda}', \quad (11)$$

where  $\Sigma = 3 \times 10^6 \alpha^{-4/5} M_{\bullet,6}^{1/5} \dot{m}^{3/5} (\eta/0.1)^{-3/5} r^{-3/5} (1 - \sqrt{r_{\text{in}}/r})^{3/5} \text{ g cm}^{-2}$  is the surface density of the disk with  $\dot{m} = \dot{M}/\dot{M}_{\text{Edd}}$ ,  $\Omega$  is the angular velocity,  $\hat{\lambda}'$  is a unit vector paralleled to  $\mathbf{L}'(r)$  (Franchini et al. 2016). The disk size is assumed to be twice the tidal radius,

i.e.,  $r_{\text{out}} = 2r_{\text{tid}}/r_g = 94M_{\bullet,6}^{-2/3}$ .

Before  $\dot{M}_{\text{fb}} \leq \dot{M}_{\text{Edd}}$ , the disk can still be warped, and the warp may propagate back and forth steadily inside the disk if  $\alpha \lesssim H/R$  (the bending wave regime; see Nelson & Papaloizou 1999). The behavior of the warp as a function of radius and time has been studied extensively, and it is quite well understood in the diffusive regime ( $\alpha > H/R$ ) though there are still lots of work to do in the bending wave regime (see Nixon & King 2016, for a review). For the disk formed by a TDS, however, the warp could be small. It is therefore reasonable to assume that the disk angular momentum at different radii has the same direction at least in the initial super-Eddington stage (see Franchini et al. 2016), though further studies are needed to confirm this. In this case, the disk is assumed to precess globally as a rigid body with a frequency (Franchini et al. 2016; Stone & Loeb 2012)

$$\Omega_{\text{p}} = \frac{\int_{r_{\text{in}}}^{r_{\text{out}}} \Omega_{\text{LT}} L(r) 2\pi r dr}{\int_{r_{\text{in}}}^{r_{\text{out}}} L(r) 2\pi r dr}, \quad (12)$$

where the local LT precession frequency  $\Omega_{\text{LT}} = c^3(4ar^{-3/2} - 3a^2r^{-2})/2GM_{\bullet}(r^{3/2} + a)$ . If a TDS disk orbits on a plane with normal direction  $(\theta', \phi')$  in the  $Ox'y'z'$  frame at time  $t$ , after a time-step  $\delta t$ ,  $\phi'$  becomes  $\phi'(t + \delta t) = \phi'(t) + \Omega_{\text{p}}\delta t$  due to global precession, while  $\theta'$  keeps the same.

**(ii) Alignment:** An initial inclined disk will be gradually dragged to the equatorial plane of the MBH owing to the disk viscosity, leading to an alignment between the angular momenta of the disk and MBH. Franchini et al. (2016) have shown that the alignment timescale  $t_{\text{al}}$  depends on the MBH mass and spin, and they find that their results are consistent with that obtained by the method provided in Foucart & Lai (2014). Franchini et al. (2016) showed that  $t_{\text{al}} \propto 10^{-3.7a}$  for  $10^7 M_{\odot}$  MBHs in their Figure 12, and we further find that  $t_{\text{al}} \propto M_{\bullet}^{0.35}$  according to Equation (35) in Foucart & Lai (2014). Combining the above two results,  $t_{\text{al}}$  can be approximated as

$$\log(t_{\text{al}}/\text{day}) \sim -3.7a + 3.9 + 0.35(\log M_{\bullet,6} - 1), \quad (13)$$

for a disk with a fixed viscosity parameter  $\alpha = 0.1^4$ . The alignment timescale can range from days to years depending on the MBH spin, and the higher the spin, the faster the alignment. The viscous time [ $t_{\text{vis}} \sim \alpha^{-1}(GM_{\bullet}/R^3)^{-1/2}(H/R)^{-2}$ ] at the outer disk edge is on the order of years for the super-Eddington stage (Strubbe & Quataert 2009), which could be longer or comparable to the alignment timescale. The time for the accretion rate to decline to sub-Eddington value is about the same order, which means the disk could still be inclined in some cases when the disk becomes thin and enters the diffusive regime.

With the assumptions made above, the projected disk angular momentum per unit area in the  $x'y'$ -plane ap-

<sup>4</sup> According to Franchini et al. (2016),  $t_{\text{al}} \propto \alpha^{-1}$ . Therefore, we have also checked whether our results on the spin distributions are affected by choosing a different  $\alpha$  and find that choosing an  $\alpha$  a few times smaller or larger introduces insignificant effect to the resulting spin distributions.

proximately evolves as

$$L'_{xy} = L'_{xy,0} \exp(-t/t_{\text{al}}), \quad (14)$$

where  $L'_{xy,0}$  is the initial value (Franchini et al. 2016).

### 2.1.3. Numerical method to solve the MBH spin evolution equation

In this sub-section, we introduce the numerical method to solve Equation (1), and Equation (2) or (3). As discussed above, the disk formed by each TDS is initially thick in geometry due to super-Eddington accretion. In this stage, the disk is assumed to precess globally and gradually align with the MBH equatorial plane. After that, the disk becomes thin when the accretion rate declines to  $\dot{M}_{\text{Edd}}$ , and there are two possibilities: (1) the disk angular momentum is already aligned with the MBH spin; (2) the disk is not aligned yet and will be warped under the diffusive regime. For the second case, if the warp radius exceeds the disk size, then the disk angular momentum is assumed to be simultaneously aligned with the MBH spin. Following Perego et al. (2009), the rapid temporal evolution of the warped disk is separated from the longer temporal evolution of the MBH. In particular, the disk is assumed to transit through a sequence of steady states over a period of  $n\delta t < t < (n+1)\delta t$  before the alignment of disk and MBH angular momenta (adiabatic approximation). Here  $\delta t \ll t_{\text{al}}$ , and  $n$  is an integer of 0, 1, 2, .... Within each time-step  $\delta t$ , the inclination angle  $i$  is approximately unchanged, and  $E_{\text{in}}$  and  $L_{\text{in}}$  can be estimated according to the array obtained in Section 2.1.1.

The spin direction of an MBH is described by  $\theta_{\bullet}$  and  $\phi_{\bullet}$  with respect to the observer in the  $Oxyz$  frame. Then the MBH angular momentum can be expressed as  $\mathbf{J} = (J_x, J_y, J_z) = J(\sin\theta_{\bullet}\cos\phi_{\bullet}, \sin\theta_{\bullet}\sin\phi_{\bullet}, \cos\theta_{\bullet})$ , and  $\mathbf{J}'$  can be related to  $\mathbf{J}$  by a rotation matrix  $\mathcal{R}_{ij}$  ( $i, j=1, 2, 3$ ), i.e.,  $\mathbf{J}' = \mathbf{J}\mathcal{R} = [0, 0, J]$ . Similarly, for a TDS orbiting with angular momentum direction  $\theta$  and  $\phi$  relative to the observer, the angular momentum per unit area is described by  $\mathbf{L} = L(\sin\theta\cos\phi, \sin\theta\sin\phi, \cos\theta)$ , and  $\mathbf{L}' = L'\mathcal{R} = \mathbf{L}\mathcal{R}$ , from which the unit vector  $\hat{\mathbf{l}}' = (\hat{l}'_x, \hat{l}'_y, \hat{l}'_z)$  can be derived. This corresponds to an inclination angle  $i = \theta' = \arccos(\hat{l}'_z)$  between the disk and MBH angular momenta, and an azimuthal angle  $\phi' = \arccos\left(\hat{l}'_x/\sqrt{\hat{l}'_x{}^2 + \hat{l}'_y{}^2}\right)$  in the  $Ox'y'z'$  reference frame.

Considering Equation (2) in the  $Ox'y'z'$  frame, within  $\delta t$ , the spin change in terms of three components  $\delta\mathbf{J}' = (\delta J'_x, \delta J'_y, \delta J'_z)$  can be calculated through

$$\begin{aligned} \delta J'_x &\approx \delta t \left[ \dot{M}r_g c L_{\text{in}} \hat{l}'_x + \frac{4\pi G J}{c^2} \int_{\text{disk}} \frac{L'_y(r)}{r^2 r_g} dr \right], \\ \delta J'_y &\approx \delta t \left[ \dot{M}r_g c L_{\text{in}} \hat{l}'_y - \frac{4\pi G J}{c^2} \int_{\text{disk}} \frac{L'_x(r)}{r^2 r_g} dr \right], \\ \delta J'_z &\approx \delta t \left[ \dot{M}r_g c L_{\text{in}} \hat{l}'_z \right]. \end{aligned} \quad (15)$$

The spin variation in the observer's  $Oxyz$  frame can be obtained via  $\delta\mathbf{J} = \delta\mathbf{J}'\mathcal{R}^{-1}$ . In the next time-step,  $\phi'$  of the disk angular momentum is updated due to the global precession, and the inclination angle  $i$  is updated

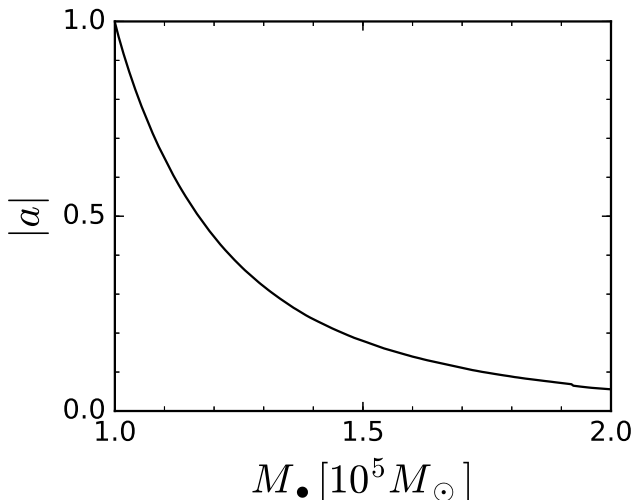


FIG. 2.— Spin evolution due to consecutive accretion of TDSs for an MBH with initial conditions of  $M_{\bullet,0} = 10^5 M_{\odot}$  and  $a_0 = 0.998$ . The MBH mass is used as a surrogate of accretion time.

owing to the exponential decline of  $L'_{xy}$  with time (see Section 2.1.2), i.e.,

$$i = \arccos\left(\sqrt{1 - L'^2_{xy}/L'^2}\right). \quad (16)$$

This leads to an update of  $\hat{\mathbf{I}}' = (\sin i \cos \phi', \sin i \sin \phi', \cos i)$ , and Equation (15) is solved once again. The above procedures are repeated until  $|\cos i'|$  is close to 1 or the accretion rate falls below the Eddington limit.

If the disk angular momentum is still not aligned with the MBH spin when  $\dot{M}_{\text{fb}} < \dot{M}_{\text{Edd}}$ , then the disk enters the diffusive regime and warps. The disk is maximally warped at around the warp radius  $r_{\text{warp}}$  (see Perego et al. 2009, for detailed expression of  $r_{\text{warp}}$ ). If the disk size is larger than  $r_{\text{warp}}$ , then the spin evolution is still described by Equation (2), where  $\hat{\mathbf{I}}$  is now parallel with the MBH spin. The analytical solution for the disk profile that describes how the disk is warped at different radii is given in Martine et al. (2007) relative to the MBH coordinate, and the analytical expression of the torque term in Equation (2) is directly given by Perego et al. (2009, see their Appendix) in the  $Ox'y'z'$  frame, which is then rotated back to the  $Oxyz$  frame. However, if the warp radius exceeds the disk size, i.e.,  $r_{\text{warp}} > r_{\text{out}}$ , which means there is no warp in the disk, then the MBH and the disk are assumed to be instantaneously aligned (or anti-aligned) with each other (for the criterion for anti-alignment, see Section 2; see also King et al. 2005). For both cases, the second term on the r.h.s. of Equation (2) reduces to 0. Then we only need to solve Equation (3) governing the spin magnitude evolution, and the spin direction is realigned to that of  $\mathbf{J}_{\text{disk}} + \mathbf{J}_{\bullet}$ . For the TDS accretion,  $r_{\text{warp}} > r_{\text{out}}$  is frequently satisfied when  $\dot{M}_{\text{fb}} < \dot{M}_{\text{Edd}}$ .

Figure 2 shows the spin evolution of an MBH with its mass increase due to consecutive accretion of TDSs. Here we only show the evolution of the absolute spin value  $|a|$ , though the spin direction also evolves with time. The orbital orientations of the injected TDSs are assumed to be randomly distributed, which can result in almost the same probability for initial prograde and retrograde ac-

cretion.<sup>5</sup> About half of the TDSs should be accreted onto the central MBH via prograde direction and the MBH spin increases during each of those accretion events. The other half are accreted onto the MBH via retrograde direction and the MBH spin decreases in this case. The injection of negative angular momentum is more efficient than that of the positive one because the inner disk radius for a retrograde orbit is larger than that for a prograde orbit (see Fig. 1). Therefore, the MBH spin appears to be quickly spun down to  $\sim 0$  when the MBH mass increases by a factor of  $\sim 2$  due to consecutive accretion of TDSs. During the period of a single prograde TDS accretion, the MBH spin does increase, but the total amount of the accreted mass in a single prograde TDE is too small and thus the spin increase is too slight to be clearly shown in Figure 2.

## 2.2. Chaotic accretion via thin disk

AGN-like nuclear activities may contribute significantly to the growth of MBHs with mass  $\sim 10^6 M_{\odot}$ , as many AGNs are detected with central MBH mass around this value. Therefore, we also consider their effects on the spin evolution of the central MBHs.

Observations of maser disks, molecular clouds, and Galactic star clusters may provide clues about the gas-cloud mass in individual AGN accretion episode. The sub-pc maser disk in NGC 4258, with a  $\sim 4 \times 10^7 M_{\odot}$  MBH (Menezes et al. 2018), is estimated to have a mass in the range from  $\sim 10^4 M_{\odot}$  to  $\sim 10^6 M_{\odot}$  (e.g., Herrnstein et al. 1998, 2005). IC 2560 hosts a  $\sim 3 \times 10^6 M_{\odot}$  MBH and a maser disk of size  $\sim 0.2$  pc (Yamauchi et al. 2012). According to the estimated accretion rate of IC 2560 ( $\sim 10^{-5} M_{\odot} \text{ yr}^{-1}$ ; Ishihara & Nakai 2002), the disk mass is about  $10^4 M_{\odot}$  assuming the standard thin disk model (Shakura & Sunyaev 1973). For the  $4 \times 10^6 M_{\odot}$  MBH in our own Galactic center, observations suggest that it was active six million years ago and the mass of the disk in that accretion episode is  $\gtrsim 10^4 M_{\odot}$  (e.g., Nayakshin & Cuadra 2005; Levin & Beloborodov 2003; Paumard et al. 2006; Lu et al. 2009). In addition, star clusters in the Galactic center such as Arches and Quintuplet are found to have mass of  $\sim 10^4 M_{\odot}$  (e.g., Figer et al. 1999; Habibi et al. 2013). Dynamical simulations also suggests that the underlying stellar mass of Arches is well within  $10^4 M_{\odot}$  and  $10^5 M_{\odot}$  (e.g., Harfst et al. 2010). These findings indicate that the molecular clouds which later collapse and form those star clusters probably have the masses  $\gtrsim 10^4 M_{\odot}$ . Moreover, observations found that the molecular clouds in our Milky Way typically have masses  $\sim 10^4$ - $10^6 M_{\odot}$  (for a review see Heyer & Dame 2015).

The above lines of observational constraints on gas-cloud and disk masses may suggest that the gas-cloud mass in each AGN accretion episode is in the range of  $10^4$ - $10^6 M_{\odot}$ . One may note that the accretion disk may not be too massive, otherwise it may fragment into clumps against its own gravity (Kolykhalov & Sunyaev 1980; Goodman 2003; King & Pringle 2007). The self-

<sup>5</sup> Note that the cross section for the tidal disruption of retrograde stars around rapidly rotating MBHs can be somewhat larger than that of prograde stars (Beloborodov et al. 1992), which may lead to even more significant spin-down effect.

gravitating disk mass  $M_{\text{sg}}$  can be estimated via the Toomre's  $Q$  criterion, i.e., the disk size is limited by the fragmentation radius where  $Q \sim c_s \Omega / \pi G \Sigma = 1$ , with  $c_s$  the sound speed,  $\Omega$  the Keplerian angular velocity, and  $\Sigma$  the disk surface density. This results in an upper limit on the disk mass (Dotti et al. 2013), i.e.,

$$M_{\text{sg}} \approx 2 \times 10^4 \alpha_{0.1}^{-1/45} \left( \frac{f_{\text{Edd}}}{\eta_{0.1}} \right)^{4/45} M_{\bullet,6}^{34/45} M_{\odot}, \quad (17)$$

where  $\alpha_{0.1} = \alpha/0.1$  and  $\eta_{0.1} = \eta/0.1$ .

If the cloud mass is about  $10^4 - 10^5 M_{\odot}$ , either or not regulated by self-gravity, then the growth history of an MBH with final mass  $\gtrsim 10^6 M_{\odot}$  should have a number of or many AGN accretion episodes if the contribution of these phases to the mass growth is significant, and the accretion in different AGN episodes is probably chaotic, i.e., with randomly distributed inclination angles relative to the MBH spin. We therefore consider the following cases for disk mass in the AGN episodes.

(i) The whole gas-cloud collapse and form an accretion disk without mass loss, i.e.,  $M_{\text{disk}} = M_{\text{cl}}$ , where  $M_{\text{cl}}$  is set to be constant  $10^4 M_{\odot}$  or  $10^5 M_{\odot}$  for all MBHs.

(ii) The disk mass is regulated by self-gravity, i.e.,  $M_{\text{disk}} = \min(M_{\text{cl}}, M_{\text{sg}})$ , where  $M_{\text{cl}}$  is  $10^4 M_{\odot}$  or  $10^5 M_{\odot}$  for all MBHs, or randomly drawn from a flat distribution between  $10^4 M_{\odot}$  and  $10^5 M_{\odot}$  in the logarithmic space.

For both cases, the gas-cloud in each episode is assumed to fall in with random directions, and similar to the disk formed by TDSs, initially  $\mathbf{J}_{\text{disk}}$  has an azimuthal angle  $\phi$  randomly distributed, and a polar angle  $\theta$  drawn from a distribution proportional to  $\sin \theta$ . The disk is assumed to be described by the standard thin disk model, and the radial and vertical shear viscosities follow a power law, i.e.,  $\nu_1 \propto r^{3/4}$  and  $\nu_2 \propto r^{3/4}$ . For radial viscosity  $\nu_1$ , the  $\alpha$  prescription is adopted with  $\alpha = 0.09$ , and the main properties of the disk are detailed in Perego et al. (2009) and Dotti et al. (2013).

Similar to the late stage of sub-Eddington accretion of TDSs described in Section 2.1, the mass and spin evolution of MBHs are obtained by solving Equation (1) and Equation (2) or (3) with adiabatic approximation (Perego et al. 2009). The Eddington ratio  $f_{\text{Edd}}$  in Equation (1) mainly determines the mass growth rate and has little effect on the spin-mass evolutionary curves. We therefore assume a constant  $f_{\text{Edd}}$  of 0.3 for the gas-cloud accretion. As the inner disk is bent to the MBH equatorial plane due to the Bardeen-Petterson effect,  $\hat{\mathbf{l}}$  in Equation (2) is parallel to the MBH spin, and the ISCO is the value for equatorial thin disks.

Figure 3 shows the spin evolution due to chaotic accretion of gas clouds. The cloud mass is set to be constant  $10^4 M_{\odot}$  or  $10^5 M_{\odot}$  across the accretion history, and the disk mass is either or not capped by the self-gravitating mass. For an initially non-rotating MBH of  $10^5 M_{\odot}$ , all of the cases show an initial sharp increase in spin, which is due to quick alignment of MBH spin to the disk angular momentum (even if the disk is initially counter-rotating), because the disk angular momentum dominates over the MBH spin at the beginning (see also Dotti et al. 2013). With the growth of MBHs,  $\mathbf{J}_{\bullet}$  becomes comparable with  $\mathbf{J}_{\text{disk}}$  and the alignment time becomes significant with respect to the accretion time. This results in a decrease

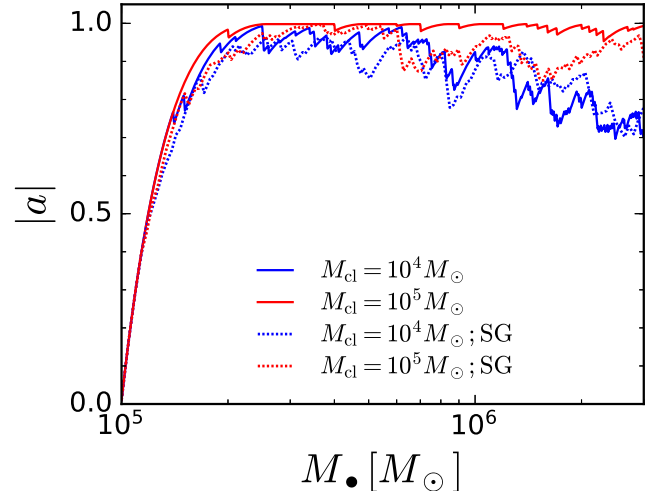


FIG. 3.— Spin evolution due to chaotic accretion of gas-cloud for initially non-spinning MBHs with  $M_{\bullet,0} = 10^5 M_{\odot}$ . The red and blue solid (or dotted) lines are for a gas-cloud mass of  $10^5 M_{\odot}$  and  $10^4 M_{\odot}$  in each gas-cloud accretion episode without (or with) consideration of disk self-gravity.

in spin more or less due to the more effective injection of negative angular momentum by counter-rotating disks. The spin-down effect is more prominent for low-mass clouds ( $10^4 M_{\odot}$ ), because the alignment of MBH spin to disk angular momentum is less efficient. If we compare the alignment timescale  $t_{\text{al}}$  (Perego et al. 2009) with the disk-consumption time  $t_{\text{acc}}$  in each episode, we find that  $t_{\text{acc}}/t_{\text{al}} \sim 5 M_{\text{cl},4} M_{\bullet,6}^{-33/35}$  by neglecting some unimportant terms. For MBHs of  $\sim 10^5 M_{\odot}$ ,  $t_{\text{acc}}/t_{\text{al}} \gg 1$ , and the alignment is efficient even for low-mass clouds ( $10^4 M_{\odot}$ ). The disk mass and size are crucial to the second term of Equation (2) and determines how efficient the alignment is. The larger the disk mass is, the higher spin the MBH maintains. Considering the self-gravity of disks does not make much difference to the spin evolution for the case with  $M_{\text{cl}} = 10^4 M_{\odot}$  though it does introduce some effect to the case with  $M_{\text{cl}} = 10^5 M_{\odot}$  because  $M_{\text{sg}}$  is substantially smaller than  $M_{\text{cl}}$  only when  $M_{\text{cl}}$  exceeds  $10^5 M_{\odot}$  at  $M_{\bullet} \sim 10^6 M_{\odot}$  (Fig. 3, and see also Fig. 11 in Zhang & Lu 2019).

### 3. MODEL SETTINGS AND MODEL RESULTS

We consider MBHs all with assumed initial masses of  $M_{\bullet,0} = 10^5 M_{\odot}$ , initial spins of  $a_0 = 0.5$ ,<sup>6</sup> and final masses of  $M_{\bullet,f} = 10^{6.5} M_{\odot}$ . They experience accretion of both gas-clouds and TDSs. During the period of gas-cloud accretion, they appear as AGNs. Our model involves two parameters, i.e.,  $f_{\text{TDE}}$  and  $M_{\text{cl}}$ , as detailed below.

(1) The parameter  $f_{\text{TDE}}$  denotes the fraction of mass growth of the final MBH contributed by TDSs, i.e.,  $f_{\text{TDE}} \equiv \Delta M_{\bullet,\text{TDE}} / (M_{\bullet,f} - M_{\bullet,0})$  with  $\Delta M_{\bullet,\text{TDE}}$  the total mass increase contributed by TDS accretion. In reality  $f_{\text{TDE}}$  may not be a constant but depend on the MBH mass and/or the environment. However, how  $f_{\text{TDE}}$  explicitly depends on MBH mass is currently unknown. As

<sup>6</sup> We have checked and found that choosing a different initial spin distribution does not significantly affect the results presented in this paper.

the main focus of this paper is to demonstrate the effect of accreting TDSs on the spin evolution of low mass MBHs ( $\sim 10^6 M_\odot$ ), it is reasonable to assume a constant  $f_{\text{TDE}}$ , at least as the mean value. Therefore, we consider three cases with fixed values of  $f_{\text{TDE}}$  for all MBHs, i.e.,  $f_{\text{TDE}} = 0.1, 0.5, \text{ and } 0.9$ , respectively. These three cases correspond to that the gas-cloud accretion dominates the MBH growth, the accretion of gas-cloud and TDSs are equally important, and the TDS accretion dominates the MBH growth, respectively. It is also plausible that  $f_{\text{TDE}}$  is different for MBHs with the same mass due to their different environments. For this reason, we also consider a case with  $f_{\text{TDE}}$  randomly distributed between 0.1 and 0.9 for those MBHs.

(2) The parameter  $M_{\text{cl}}$  denotes the gas-cloud mass available in each gas-cloud (AGN) accretion episode. Our models assume that  $M_{\text{cl}}$  is either fixed at  $10^4 M_\odot$  or  $10^5 M_\odot$  for each gas-cloud accretion episodes of all the MBHs, or it is randomly distributed over  $10^4 M_\odot$  and  $10^5 M_\odot$  for different episodes of each MBH. For those fixed  $M_{\text{cl}}$  models, the disk is either or not regulated by self-gravity (for these settings, see discussions on observational results in Section 2.2).

For an MBH with fixed  $M_{\text{cl}}$  during its accretion history, the number of gas-cloud accretion episodes is calculated through  $N_{\text{cl}} = \text{int}[(1 - f_{\text{TDE}})(M_{\bullet, \text{f}} - M_{\bullet, 0})/M_{\text{cl}}] + 1$ . We assume that each MBH starts with accreting TDSs and we ignore the intervals between any two adjacent accretion episodes. The gas-cloud accretion episodes are randomly injected into the growth history of an MBH. Specifically, we produce  $N_{\text{cl}}$  random numbers between  $M_{\bullet, 0}$  and  $M_{\bullet, \text{f}}$ . With the growth of the MBH due to TDS accretion, once the mass reaches any one of those random values, it starts a gas-cloud accretion episode and the TDS accretion is switched off. This gas-cloud accretion episode ends when the gas-cloud is all consumed, and the TDS accretion is then switched on again until the MBH mass reached another random number produced above and another gas-cloud (AGN) accretion episode is switched on.

For those cases considering disk self-gravity, the number of gas-cloud accretion is different even for accretion histories with the same  $f_{\text{TDE}}$  since  $M_{\text{sg}}$  is dependent on the MBH mass. In the modeling, we randomly produce 1, 2, 3, ... random numbers between  $M_{\bullet, 0}$  and  $M_{\bullet, \text{f}}$ , calculate  $M_{\text{sg}}$  and  $M_{\text{disk}} = \min(M_{\text{sg}}, M_{\text{cl}})$  for each random number produced, and get the sum of those disk masses. The above procedures are terminated once the summation of the disk masses exceeds  $(1 - f_{\text{TDE}})(M_{\bullet, \text{f}} - M_{\bullet, 0})$ . Then the accretion history of the MBH is known, i.e., when the MBH starts a period of gas-cloud accretion, and how massive the disk mass is in each episode. Therefore, different models have different numbers of gas-cloud accretion episodes. For a model even with a fixed  $N_{\text{cl}}$ , the accretion histories of individual MBHs are still different from each other since the TDS and gas-cloud accretion episodes are injected into the accretion history randomly and each with a random orientation (see Section 2).

According to our settings, we have 20 models in total (see Table 2). For each model, we calculate the mass and spin evolution for 500 MBHs according to the methodology described in Section 2. From each of the evolutionary curve, we randomly select 1000 mock AGNs with

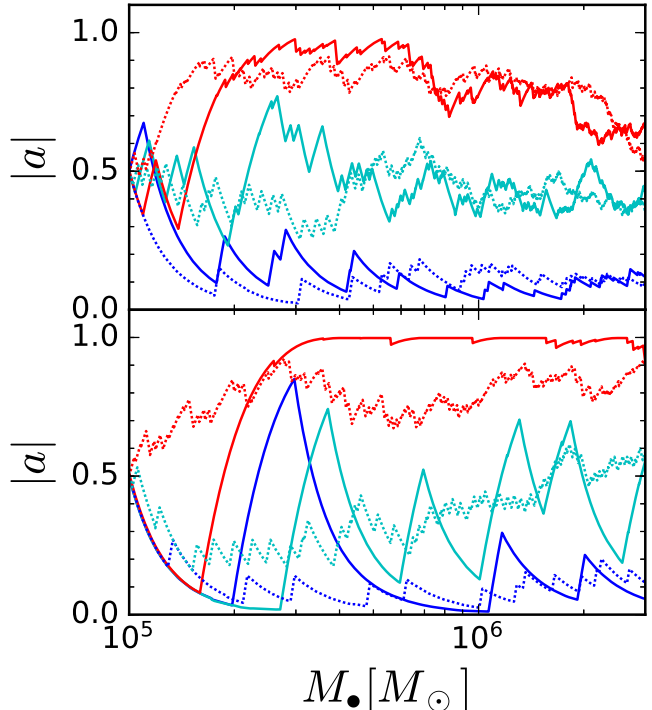


FIG. 4.— Examples of spin evolutionary curves. The gas-cloud in each AGN accretion episode is  $10^4 M_\odot$  ( $10^5 M_\odot$ ) in the top (bottom) panel, and the solid (or dotted) lines in each panel are for disks without (or with) consideration of self-gravity. The fraction of MBH mass growth contributed by TDSs is set as 10% (red), 50% (cyan), or 90% (blue).

$M_\bullet \sim 10^{5.5} - 10^{6.5} M_\odot$ , and we also randomly select 1000 mock TDEs with the same mass range. According to these procedures, the differential spin distribution of the MBHs in both the mock AGNs and TDEs can be obtained, i.e.,  $dn/da = N_{\text{tot}}^{-1} \Delta N / \Delta a$ . Here  $N_{\text{tot}} = 500,000$  is the total number of objects included in the mock sample(s), and  $\Delta N$  is the number of MBHs with spins between  $a$  and  $a + \Delta a$ .

Figure 4 shows some spin evolutionary curves, as examples, for MBHs experiencing both TDS and AGN accretion episodes, with different  $f_{\text{TDE}}$  and  $M_{\text{cl}}$ , and with or without consideration of self-gravity in the gas-cloud accretion phase. As shown in this figure, those MBHs are spun up in the episodes of gas-cloud accretion and the MBH spins can increase to large values in a single gas-cloud accretion episode when the disk is massive (e.g.,  $10^5 M_\odot$ ) and the disk self-gravity is ignored, while the MBHs are spun down significantly after the accretion of a large number of TDSs. This is because each TDS adds at most  $\sim 0.5 M_\odot$  to the MBH mass, while a gas-cloud accretion episode adds  $\sim 10^4 - 10^5 M_\odot$ . Therefore, the angular momentum of the TDS is tiny compared to the MBH spin, and the probability of co- or counter-alignment to the MBH spin is essentially the same for the disk angular momentum. Gas-clouds, however, have much higher (orbital) angular momenta, which can dominate over that of the MBH, and therefore the MBH spin tends to co-align with the disk angular momentum. For a larger  $M_{\text{cl}}$  ( $> 10^5 M_\odot$ ), the alignment of the MBH spin to the disk angular momentum is more efficient, and the spin can reach even higher values in a single chaotic accretion episode. How the MBH spin evolves depends on the rel-

TABLE 1  
SPIN MEASUREMENTS OF INDIVIDUAL AGNS VIA FE K $\alpha$  LINES.

Object name	$M_{\bullet}(10^6 M_{\odot})$	Spin
1H 0707-495	$\sim 2.3$	$> 0.97$
Ark 564	$\sim 1.1$	$0.96^{+0.01}_{-0.07}$
MCG 6-30-15	$2.9^{+1.8}_{-1.6}$	$> 0.98$
Mrk 359	$\sim 1.1$	$0.66^{+0.30}_{-0.54}$
NGC 1365	$\sim 2$	$\geq 0.84$
NGC 4051	$1.91 \pm 0.78$	$> 0.99$

NOTE. — This table lists those individual AGNs with spin measurements that have MBH mass in the range of  $10^6 - 10^{6.5} M_{\odot}$ , selected from Brenneman (2013) and Reynolds (2014). References for those spin measurements are Zoghbi et al. (2010) for 1H 0707-495, Walton et al. (2013) for Ark 564 and Mrk 359, Brenneman & Reynolds (2006) for MCG 6-30-15, Risaliti et al. (2013) for NGC 1365, and Patrick et al. (2012) for NGC 4051, respectively. The mass measurements for them are adopted from Zhou & Wang (2005) (1H 0707-495, Ark 564 and Mrk 359), McHardy et al. (2005) (MCG 6-30-15), Risaliti et al. (2009) (NGC 1365), and Peterson et al. (2004) (NGC 4051).

ative contribution from accretion of TDSs to the MBH mass growth. If  $f_{\text{TDE}} = 0.1$ , the MBH spin can maintain at high values at later stages when  $M_{\bullet} \gtrsim 10^6 M_{\odot}$ ; if  $f_{\text{TDE}} = 0.9$ , the MBH spin may be always close to 0 when  $M_{\bullet} \gtrsim 10^6 M_{\odot}$ . However, if considering the disk self-gravity, the probability for MBHs to be spun up to large values may be significantly suppressed in a single gas-cloud accretion episode, especially for those cases with  $M_{\text{cl}} \gtrsim 10^5 M_{\odot}$ , because the disk mass is limited to about  $M_{\text{sg}} \sim 10^4 M_{\odot}$  at  $M_{\bullet} \sim 10^6 M_{\odot}$ . This would lead to a lack of mock MBHs with spins close to the maximum spin value as will be shown in Figure 6.

Figure 5 shows differential (top panels) and cumulative (bottom panels) distributions of spins for those mock samples of MBHs selected in the gas-cloud (AGN) accretion episodes, according to the mass and spin evolutionary curves obtained from our simulations by setting different  $f_{\text{TDE}}$  and  $M_{\text{cl}}$  without consideration of disk self-gravity. Here we show both the prograde-spin accretion ( $a > 0$ ) and retrograde one ( $a < 0$ ). It appears that retrograde-spin accretion is almost negligible for all models simply because the alignment timescale is short and anti-alignment cases rarely occur. If  $M_{\text{cl}} = 10^4 M_{\odot}$  (left panels), the MBH spin distribution peaks at high ( $\sim 0.6 - 1$ ), intermediate ( $\sim 0.4$ ), and low values ( $\sim 0.1$ ) for those cases with  $f_{\text{TDE}} = 0.1, 0.5$ , and  $0.9$ , respectively, while the MBH spins cover a broad range from 0 to 1 and the distribution is roughly flat from 0.2 to 0.6 when  $f_{\text{TDE}}$  is randomly distributed between 0.1 and 0.9. If  $M_{\text{cl}} = 10^5 M_{\odot}$  (right panels), the spin increase during a single AGN episode is more significant than that for  $M_{\text{cl}} = 10^4 M_{\odot}$ . Therefore, the resulting spin distributions shift towards higher spin values compared with those corresponding cases of  $M_{\text{cl}} = 10^4 M_{\odot}$ , although the accretion of TDSs is still efficient in slowing the rotation of the central MBH. In the case of  $M_{\text{cl}} = 10^5 M_{\odot}$ , the spin distribution peaks at a value close to 1 with a skewed wing towards 0 when  $f_{\text{TDE}} = 0.1, 0.5$ , or randomly distributed between 0.1 and 0.9, while the spins concentrate at lower values  $\lesssim 0.3$  when  $f_{\text{TDE}} = 0.9$ . The median spin values of those mock AGNs generated with different model parameters ( $f_{\text{TDE}}, M_{\text{cl}}$ ) are listed in Table 2, which will be compared with the simulation results obtained in Section 4.

According to the comparison between the left and right panels of Figure 5, choosing an  $M_{\text{cl}}$  substantially larger than  $10^5 M_{\odot}$ , which means only one or a few gas-cloud (AGN) accretion episodes, will lead to the spins more concentrated at higher values for  $f_{\text{TDE}} = 0.1, 0.5$ , or  $f_{\text{TDE}}$  randomly distributed over the range from 0.1 to 0.9, and the peak of spin distribution resulting from the case with  $f_{\text{TDE}} = 0.9$  shifts towards an even higher value.

For comparison, we plot Figure 6 to show the results for those cases with disk mass capped by the self-gravity constraint, considering a constant gas-cloud mass of  $10^4 M_{\odot}$  or  $10^5 M_{\odot}$  for all MBHs, or a gas-cloud mass randomly selected in the range of  $10^4 - 10^5 M_{\odot}$  for each AGN accretion episode. All of these cases show similar spin distribution as that for  $M_{\text{disk}} = M_{\text{cl}} = 10^4 M_{\odot}$  (left panels in Fig. 5). This is because  $M_{\text{sg}}$  is comparable to  $M_{\text{cl}}$  when  $M_{\bullet} \sim 10^6 M_{\odot}$  as mentioned above to explain Figure 4. If considering disk self-gravity, a gas-cloud with mass much larger than  $10^4 M_{\odot}$  forms a disk of  $\sim 10^4 M_{\odot}$ . This is the reason why the spin distribution indicated by the thick red dotted-line in the right panel of Figure 6 does not peak at  $\sim 1$ , apparently different from the one without considering the disk self-gravity (thin red dotted-line).

Note that in our models we do not set gas-cloud mass  $\lesssim 10^3 M_{\odot}$  as observations hint larger disk mass (see discussion in Section 2.2). However, if the gas-cloud mass is smaller than  $10^3 M_{\odot}$  and the disk-to-MBH mass ratio is  $\lesssim 10^{-3}$  for  $\sim 10^6 M_{\odot}$  MBHs, then MBHs cannot be spun up to large values (e.g.,  $\lesssim 0.4$ ; see the analytic analysis in King et al. 2008 and Fig. 11 in Zhang & Lu 2019) either in a single gas-cloud accretion episode or after a large number of chaotic accretion episodes, and this will result in a spin distribution oscillating around a small value with a scatter determined by the disk-to-MBH mass ratio and  $f_{\text{TDE}}$  (e.g., see Figs. 3 and 4 in King et al. 2008). Our calculations further show that significant TDS accretion would lead to not only smaller spins but also a narrower spin distribution for a given disk-to-MBH mass ratio, i.e., the larger the  $f_{\text{TDE}}$ , the smaller the spin values and its scatter, which is basically the difference that may be used to distinguish TDS accretion from small gas-cloud (with mass  $\gtrsim 10^3 M_{\odot}$ ) accretion (e.g., Figs. 5 and 7).

Figure 7 shows differential and cumulative distributions of spins for those mock samples of MBHs selected in the TDS accretion phases, also according to the mass and spin evolutionary curves obtained from our simulations by setting different  $f_{\text{TDE}}$  and  $M_{\text{cl}}$  without consideration of disk self-gravity. Now the prograde and retrograde spins are almost symmetrically distributed. The reason is that the alignment timescale is short and the probability for anti-alignment is almost the same as that for alignment because  $|\mathbf{J}_{\text{disk}}|$  is much smaller than  $|\mathbf{J}_{\bullet}|$ . For those cases with  $M_{\text{cl}} = 10^4 M_{\odot}$  (left panels), the spin distribution peaks at  $\pm 0.1, \pm 0.4$ , and  $\pm 0.7$  when  $f_{\text{TDE}} = 0.9, 0.5$ , and  $0.1$ , respectively, while it covers a broad range from -1 to 1 and the distribution is rather flat in the range of  $0.2 < |a| < 0.6$  when  $f_{\text{TDE}}$  is randomly distributed between 0.1 and 0.9. For those cases with  $M_{\text{cl}} = 10^5 M_{\odot}$  (right panels), the spins  $|a|$  are more concentrated at high ( $\gtrsim 0.8$ ) or low values ( $\lesssim 0.2$ ) when  $f_{\text{TDE}} = 0.1$  or  $0.9$ , while it is close to a flat distribution over the range from 0 to 1 when  $f_{\text{TDE}} = 0.5$  or

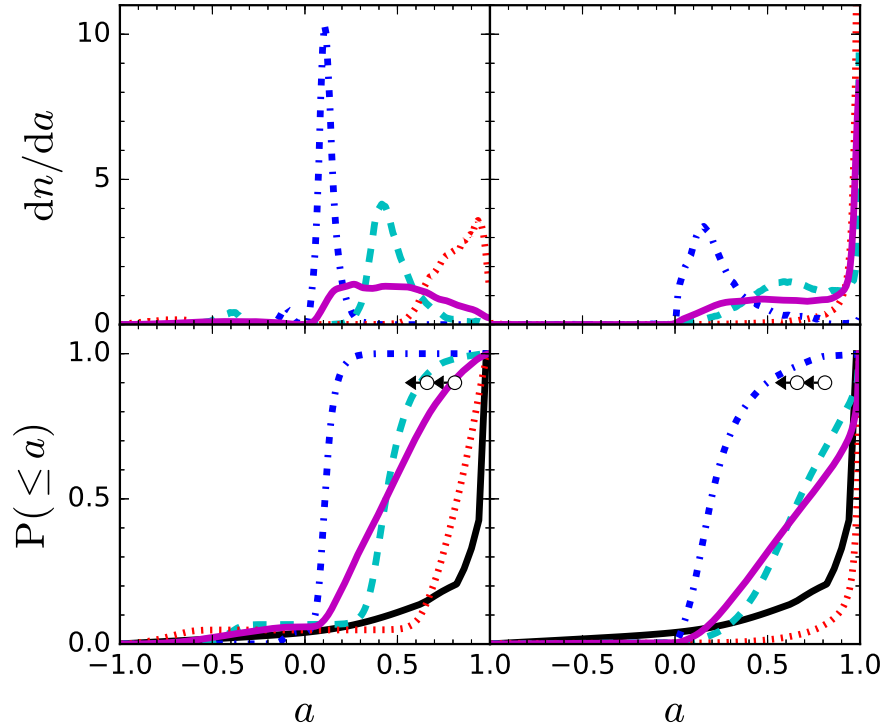


FIG. 5.— Differential (upper panels) and cumulative (lower panels) spin distributions of those mock MBHs “detected” in the gas-cloud (AGN) accretion episodes obtained from simulations for different models. Left (right) panels represent models with fixed cloud mass of  $10^4 M_\odot$  ( $10^5 M_\odot$ ) in each AGN episode. The fraction of MBH mass growth due to TDS accretion is set as 10% (red dotted), 50% (cyan dashed), 90% (blue dot-dashed) or randomly distributed between 10% to 90% over different MBHs (solid magenta). The black line shows the cumulative spin distribution inferred from spin measurements listed in Table 1, where the errors have been taken into account. The open circles represent the constraints on the effective spin obtained from the stacked X-ray spectrum of 51 NLS1s, i.e.,  $a < 0.81$  or  $< 0.66$  at the 90% confidence level, presented in Liu et al. (2015).

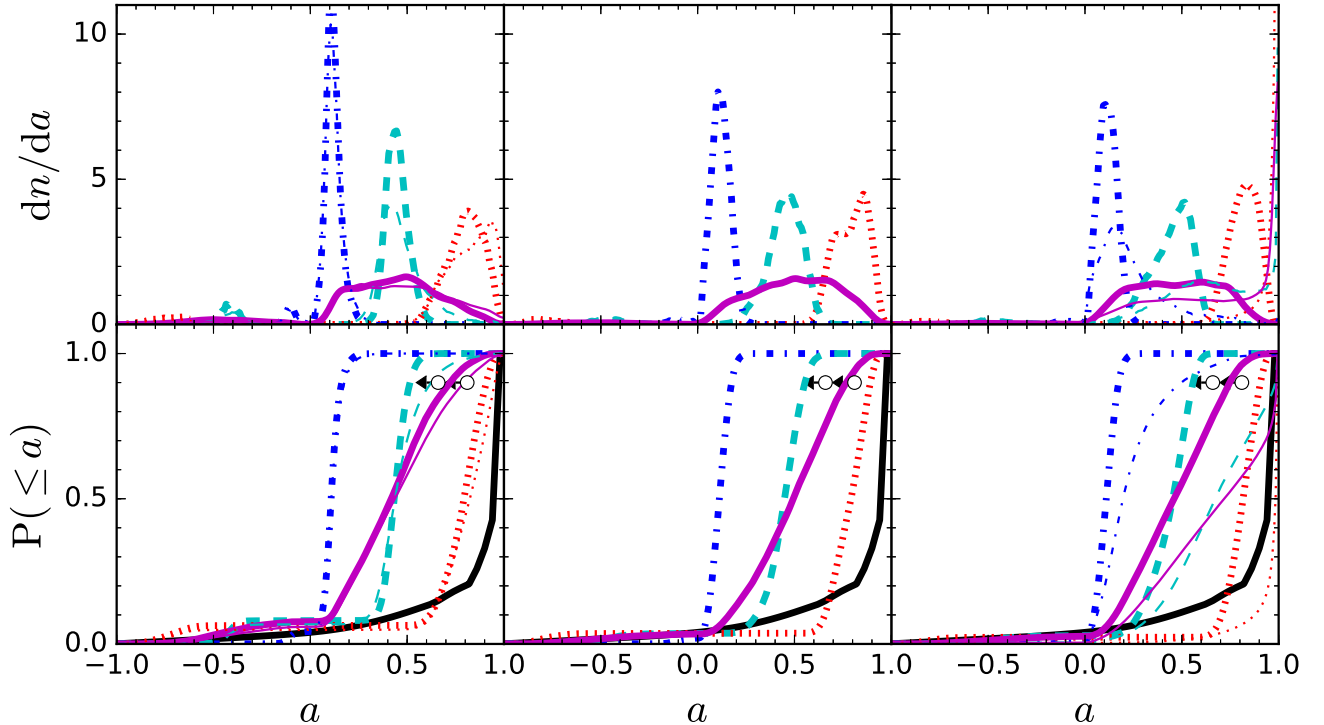


FIG. 6.— Legend similar to Figure 5. Thick curves in each panel represent the results obtained from those models by considering the self-gravity regulation of the disks in the gas-cloud accretion episodes, i.e.,  $M_{\text{disk}} = \min(M_{\text{sg}}, M_{\text{cl}})$  (see Table 2). Left and right panels show the cases with assumption of  $M_{\text{cl}} = 10^4 M_\odot$  and  $10^5 M_\odot$ , respectively; middle panels show the cases with assumption of  $M_{\text{cl}}$  randomly distributed over  $10^4 M_\odot$  and  $10^5 M_\odot$ . For comparison, the results shown in Fig. 5 for models without considering the self-gravity regulation of the disks are also correspondingly shown here by thin curves in the left and right panels.

TABLE 2  
 MEDIAN SPIN VALUES OF MOCK AGNs WITH MASS  $\sim 10^6 M_\odot$  PREDICTED FROM OUR MODELS AND THE EFFECTIVE SPINS OBTAINED FROM THE STACKED ‘NLS1’ X-RAY SPECTRA ASSUMING THE MODEL SPIN DISTRIBUTIONS.

$f_{\text{TDE}}$	$M_{\text{cl}}(M_\odot)$	Without SG		With SG	
		med-Spin	eff-Spin	med-Spin	eff-Spin
0.1	$10^4$	$0.83^{+0.11}_{-0.15}$	$0.67^{+0.27}_{-0.49}$	$0.80^{+0.09}_{-0.13}$	$0.77^{+0.20}_{-0.40}$
0.5	$10^4$	$0.44^{+0.13}_{-0.09}$	$0.50^{+0.35}_{-0.41}$	$0.44^{+0.06}_{-0.06}$	$0.31^{+0.33}_{-0.31}$
0.9	$10^4$	$0.11^{+0.05}_{-0.04}$	$0.27^{+0.40}_{-0.27}$	$0.11^{+0.04}_{-0.03}$	$0.21^{+0.34}_{-0.21}$
ran(0.1-0.9)	$10^4$	$0.44^{+0.28}_{-0.26}$	$0.50^{+0.34}_{-0.40}$	$0.42^{+0.23}_{-0.25}$	$0.37^{+0.37}_{-0.22}$
0.1	$10^5$	$0.99^{+0.01}_{-0.05}$	$0.71^{+0.29}_{-0.46}$	$0.82^{+0.07}_{-0.08}$	$0.69^{+0.22}_{-0.34}$
0.5	$10^5$	$0.68^{+0.28}_{-0.25}$	$0.60^{+0.31}_{-0.49}$	$0.46^{+0.08}_{-0.14}$	$0.43^{+0.21}_{-0.34}$
0.9	$10^5$	$0.20^{+0.21}_{-0.11}$	$0.21^{+0.40}_{-0.21}$	$0.11^{+0.05}_{-0.05}$	$0.23^{+0.30}_{-0.23}$
ran(0.1-0.9)	$10^5$	$0.72^{+0.27}_{-0.40}$	$0.53^{+0.32}_{-0.50}$	$0.46^{+0.24}_{-0.25}$	$0.50^{+0.32}_{-0.34}$
0.1	ran( $10^4$ - $10^5$ )	.....	.....	$0.80^{+0.08}_{-0.11}$	$0.71^{+0.25}_{-0.30}$
0.5	ran( $10^4$ - $10^5$ )	.....	.....	$0.45^{+0.09}_{-0.10}$	$0.49^{+0.22}_{-0.30}$
0.9	ran( $10^4$ - $10^5$ )	.....	.....	$0.12^{+0.05}_{-0.05}$	$0.21^{+0.28}_{-0.21}$
ran(0.1-0.9)	ran( $10^4$ - $10^5$ )	.....	.....	$0.50^{+0.22}_{-0.26}$	$0.40^{+0.35}_{-0.40}$

NOTE. — The first two columns list the model parameters  $f_{\text{TDE}}$  and  $M_{\text{cl}}$ , respectively. The third column lists the median values of the spin distributions resulting from each model (in terms of  $f_{\text{TDE}}$  and  $M_{\text{cl}}$ ) with  $M_{\text{disk}} = M_{\text{cl}}$ , without considering of disk self-gravity and fragmentation. The fourth column lists the effective spin obtained from the simulation for the stacked X-ray spectrum of 51 mock NLS1s similar to that in Liu et al. (2015) by assuming that NLS1s have relativistically broadened Fe  $K\alpha$  emission and the spin distribution of those NLS1s are the same as that from our model in the third column (see Section 4). The fifth and sixth columns list the median and effective spin values resulting from the models with the same  $f_{\text{TDE}}$  and  $M_{\text{cl}}$  as those for the third and fourth columns, but considering the disk self-gravity and fragmentation in the model (i.e.,  $M_{\text{disk}} = \min(M_{\text{cl}}, M_{\text{sg}})$ ). The superscript and subscript numbers associated with each spin value represent the 16th and 84th percentiles.

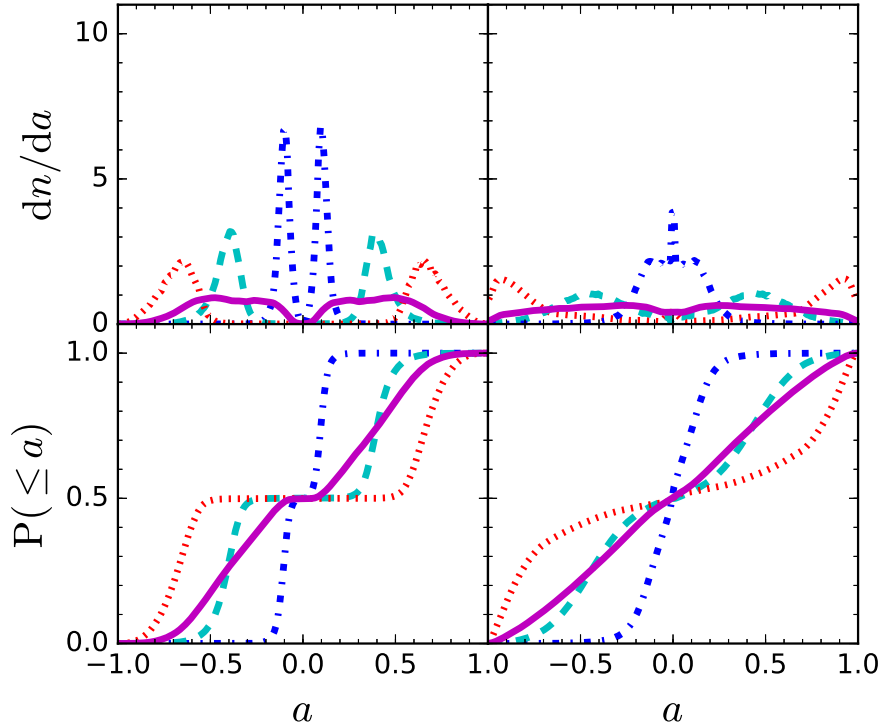


FIG. 7.— Differential (upper panels) and cumulative (lower panels) spin distributions of those mock MBHs ‘detected’ in the TDS accretion phases obtained from simulations for different models. Each of the lines in both the left and right panels represents for a model with  $M_{\text{cl}}$  and  $f_{\text{TDE}}$  the same as that shown in Fig. 5.

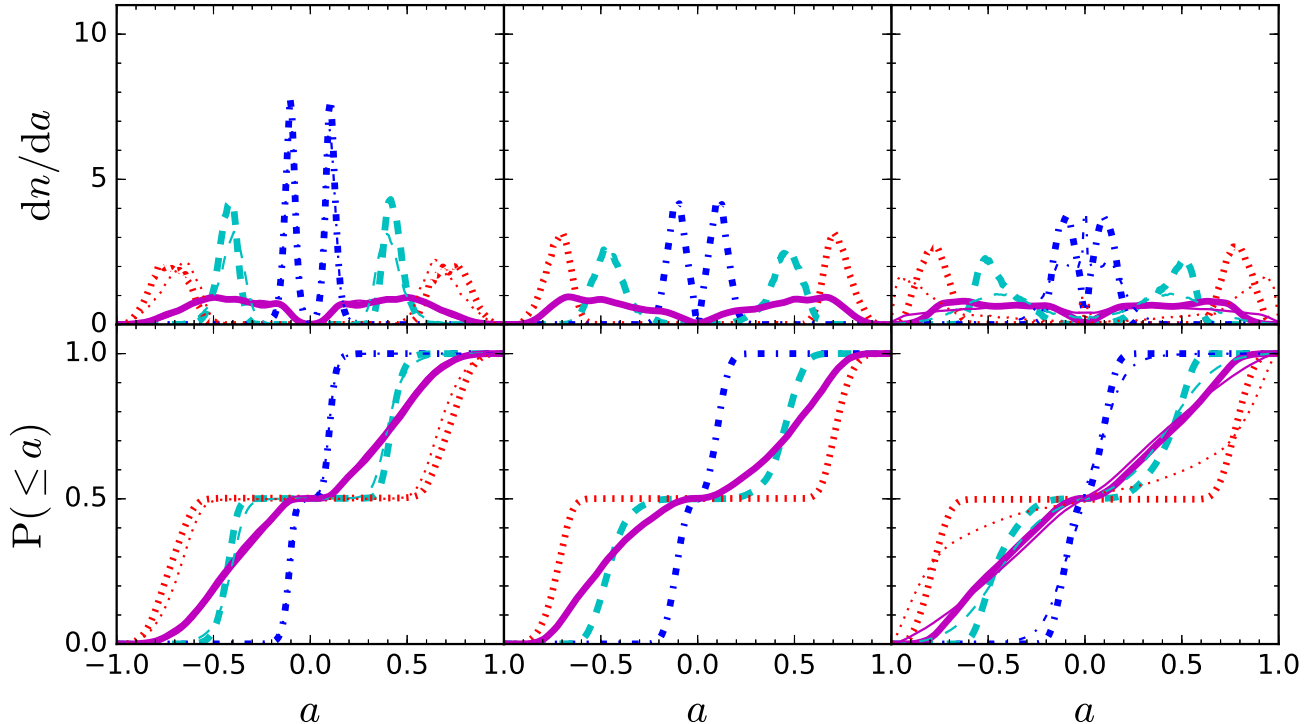


FIG. 8.— Legend similar to Figure 7. Thick curves in each panel represent the results obtained from those models by considering the self-gravity regulation of the disks in the gas-cloud accretion episodes, i.e.,  $M_{\text{disk}} = \min(M_{\text{sg}}, M_{\text{cl}})$  (see Table 2). Left and right panels show the cases with assumption of  $M_{\text{cl}} = 10^4 M_{\odot}$  and  $10^5 M_{\odot}$ , respectively; middle panels show the cases with assumption of  $M_{\text{cl}}$  randomly distributed over  $10^4 M_{\odot}$  and  $10^5 M_{\odot}$ . For comparison, the results shown in Fig. 7 for models without considering the self-gravity regulation of the disks are also correspondingly shown here by thin curves in the left and right panels.

$f_{\text{TDE}}$  is randomly set over the range from 0.1 to 0.9 for MBHs. By comparing the same type of lines shown in Figures 5 and 7 and thus the same model parameters ( $f_{\text{TDE}}, M_{\text{cl}}$ ), we can see that MBHs “detected” at the gas-cloud (AGN) accretion episodes have relatively high spins compared with those MBHs detected in the TDS accretion phase for  $f_{\text{TDE}} \gtrsim 0.5$ . For example, for the case of  $M_{\text{cl}} = 10^4 M_{\odot}$  and  $f_{\text{TDE}} = 0.1$  (0.5), half of those mock MBHs in the gas-cloud (AGN) accretion episodes have spins  $|a| > 0.83$  (0.45), while only about 7% (28%) of mock MBHs in the TDS accretion phase have spins  $|a| > 0.83$  (0.45) (see the red dotted and cyan dashed lines in the left-bottom panel of the two figures). The reason is that the decrease of MBH spin during the period of consecutive TDS accretion is more rapid than the increase of MBH spin during the AGN period when the spin is large (see Fig. 4).

Similarly, considering the self-gravity of disks during the AGN episodes results in similar spin distribution (see Figure 8) for MBHs “detected” in TDE phase as that for  $M_{\text{disk}} = M_{\text{cl}} = 10^4 M_{\odot}$  (left panels in Figure 7). Choosing an  $M_{\text{cl}}$  much larger than  $10^4 M_{\odot}$  does not affect the spin distribution when considering self-gravitating disks.

To close this section, we note here that the MBH accretion history assumed in our models is described by only two parameters, which may be too simple to reflect the reality. However, the quantitative investigation presented in the present paper on how the spin evolution is affected by the amount of mass contributed by TDSs may provide a first step for future more detailed and more realistic studies. With such a framework, future measurements of MBH spins may be used to put constraints on

the significance of TDSs accretion to  $\sim 10^6 M_{\odot}$  MBHs and also properties of gas-clouds in the AGN accretion episodes.

#### 4. IMPLICATIONS FROM CURRENT SPIN MEASUREMENTS

The spins of more than two dozen MBHs have been estimated through the profile of relativistic Fe K $\alpha$  lines detected in their X-ray spectra. According to Brenneman (2013) and Reynolds (2014), six MBHs with spin measurements from the Fe K $\alpha$  line have masses in the range of  $10^6 - 10^{6.5} M_{\odot}$ . Most of these MBHs have high spins, i.e.,  $a > 0.99$ ,  $> 0.98$ ,  $> 0.97$ ,  $0.96^{+0.01}_{-0.07}$ , and  $\geq 0.84$  for NGC 4051, MCG 6-30-15, 1H 0707-495, Ark 564, and NGC 1365, respectively. Only the small MBH ( $\sim 1.1 \times 10^6 M_{\odot}$ ) in Mrk 359 may have a relatively small spin of  $0.66^{+0.30}_{-0.54}$  (see Table 1). The cumulative distribution of those spin measurements is also shown in the bottom panels of Figure 5 and 6 (the black curve). To obtain this cumulative spin distribution, we have taken account of the error budgets of each spin measurement listed in Table 1. For each of the four objects with lower limits at 90% confidence level, we assume its spin has 90% probability to distribute uniformly in between the lower limit and the maximum spin value 0.998, and 10% probability to distribute uniformly in between  $-0.998$  and the lower limit. For each of the two spin measurements with asymmetric errors, we assume two half-Gaussians for the spin probability distribution, with the two error values the dispersions of the two Gaussian distributions, and we also adopt the cut  $|a| \leq 0.998$ . A consensus on the reliability of these spin measurements may still not be reached (e.g., Done & Jin 2016), but if these measurements are

accurate as believed and if there is no significant selection bias, then it may suggest that the contribution from TDS accretion to the growth of  $10^6 - 10^{6.5} M_\odot$  MBHs is not very significant ( $\lesssim 10\%$ ; see the bottom panels of Fig. 5 and 6).

However, the Fe  $K\alpha$  line profile measured from the stacked X-ray spectrum of 51 NLS1s indicates that the effective spin value of the MBHs in those NLS1s must be  $< 0.81$  and may be even  $< 0.66$  (at 90% confidence level) as shown in Liu et al. (2015). The two open circles with left arrows marked in Figure 5 and 6) show such constraints. As seen from Figure 5, apparently, the low effective spin may suggest that the contribution from the accretion of TDSs to the MBH growth must be comparable to or even more significant than that from the gas-cloud (AGN) accretion episodes.

To make this comparison more clear, we further simulate X-ray spectra of 51 mock AGNs similar to that in Liu et al. (2015). The X-ray spectral model used in our simulations consists of an absorbed power-law continuum and a broad Fe  $K\alpha$  line. The parameters of the continuum model for each mock AGN are taken from the best-fitting result of Liu et al. (2015) for each of those NLS1s. The broad Fe  $K\alpha$  line emission is generated by assuming a spin randomly drawn from the spin distribution resulting from each of the 20 models listed in Table 2 (see also Fig. 5 and 6)). The inclination of the disk in the broad-line model is fixed at  $30^\circ$ . The equivalent widths (EWs) of the broad lines are randomly drawn from a probability distribution constructed from the measured EW values for the two dozen sources with spin measurements listed in Brenneman (2013, two sources with extremely strong broad Fe  $K\alpha$  line, i.e.,  $EW > 600$  eV, are excluded). Then we obtain a stacked spectrum by stacking those 51 simulated X-ray spectra for each of the 20 models. The X-ray data for the majority of the mock AGNs are dominated by statistical uncertainties (low signal-to-noise ratio). In order to estimate the effective spin value as well as its uncertainty, we repeat the above simulation process, and generate 100 stacked spectra for each spin distribution. We estimate the MBH spin values (the typical  $1\sigma$  uncertainty is about  $\sim 0.3$ ) by fitting each of the 100 stacked spectra with an absorbed power-law continuum plus a relativistic broad Fe  $K\alpha$  model. The median of the 100 measured spin values is then considered as the “best-fit” effective spin value estimated from the stacked X-ray spectra for each of the 20 spin distributions resulting from those models in Section 3. The lower and upper limits of the spin values are estimated using the 16-th and 84-th percentiles (see Table 2).

For the cases without consideration of the disk self-gravity in the chaotic accretion phase, our calculations suggest that it is possible to distinguish the model with  $(f_{\text{TDE}}, M_{\text{cl}}) = (0.9, 10^4 M_\odot)$  from that with  $(f_{\text{TDE}}, M_{\text{cl}}) = (0.1, 10^4 M_\odot)$  using the X-ray spectral stacking method. The former results in a median spin value of  $a_{\text{med}} \sim 0.27$  while the latter results in a much larger value of  $a_{\text{med}} \sim 0.67$ . This is also true for those models with  $M_{\text{cl}} = 10^5 M_\odot$ , i.e.,  $a_{\text{med}} \sim 0.21$  for  $f_{\text{TDE}} = 0.9$  and  $a_{\text{med}} \sim 0.71$  for  $f_{\text{TDE}} = 0.1$ . However, we cannot distinguish the model with  $f_{\text{TDE}} = 0.5$  from that with  $f_{\text{TDE}}$  uniformly distributed over 0.1 to 0.9, i.e., the measured MBH spins are  $a_{\text{med}} \sim 0.5 - 0.6$  for

both models. For the cases considering self-gravitating disks in the chaotic phase and the three different choices of  $M_{\text{cl}}$  (the last column of Table 2), the models with  $f_{\text{TDE}} = 0.1$  and 0.9 can also be distinguished, which result in a median spin value of  $\sim 0.7$  and  $\sim 0.2$  respectively. Similarly, the models with  $f_{\text{TDE}} = 0.5$  and those with randomly distributed  $f_{\text{TDE}}$  cannot be distinguished within 20% uncertainty. Models with different choices of  $M_{\text{cl}}$  cannot be distinguished since the disk self-gravity plays a major role in determining the disk mass and thus the median spin. Consideration of disk self-gravity in general results in a smaller median spin, which is consistent with the results presented in Section 3. However, the two cases with  $(f_{\text{TDE}}, M_{\text{cl}}) = (0.1, 10^4 M_\odot)$  and  $(0.9, 10^5 M_\odot)$  by considering the disk self-gravity result in slightly larger spins than those cases without considering disk self-gravity (but they are consistent with each other within the uncertainties), which may be caused by the low signal-to-noise ratio of the simulated spectra. According to those simulation results, the observational results obtained by Liu et al. (2015) perhaps suggest that those models with  $f_{\text{TDE}} \gtrsim 0.5$  or  $f_{\text{TDE}}$  uniformly distributed over the range from 0.1 to 0.9 are favored, i.e., the accretion of TDSs contributes significantly to the mass growth of  $\sim 10^6 M_\odot$  MBHs.

Apparently the constraints on  $f_{\text{TDE}}$  obtained from the two different sets of observational results on the MBH spins are in contradiction with each other. The reason for these inconsistent constraints on  $f_{\text{TDE}}$  might be that (1) the measurements of spins for those objects listed in Table 1 may be biased towards high values, or (2) a significant fraction of those NLS1s do not have relativistic Fe  $K\alpha$  emission from the inner region of their disks, which leads to the immerse of the red wing of Fe  $K\alpha$  line in the stacked continuum and thus an underestimate of the effective spin. Future measurements of spins for a large unbiased sample of AGNs would be important in constraining the significance of the contribution from accretion of TDSs to the growth of MBHs with mass  $\sim 10^6 M_\odot$ .

## 5. CONCLUSIONS AND DISCUSSIONS

In this paper, we have quantitatively investigated the effect of accreting TDSs on the spin evolution of MBHs with mass  $\sim 10^6 M_\odot$ , by considering accretion of both TDSs and gas clouds (with several or many chaotic AGN accretion episodes). We find that the accretion of TDSs may play an important or even a dominant role in shaping the spin distribution of  $\sim 10^6 M_\odot$  MBHs, depending on the contribution fraction of the TDS accretion to the MBH growth, which is longly expected to be significant. Assuming a reasonable range for the mass of gas clouds in AGN accretion episodes, we find that most  $\sim 10^6 M_\odot$  MBHs in both the gas-cloud (AGN) and TDS accretion episodes would have: (1) low spins ( $|a| \lesssim 0.3$ ) if the contribution of TDS accretion to the growth of those MBHs is  $\gtrsim 90\%$ ; (2) high spins ( $|a| \gtrsim 0.7$ ) if this contribution is  $\lesssim 10\%$ ; and (3) intermediate spins or  $|a|$  widely distributed over the range from 0 to 1 if this contribution is intermediate or randomly distributed from 10% to 90% among those MBHs. We also find that there are fewer high-spin MBHs in the TDS accretion episodes than those in the gas-cloud accretion (AGN) episodes. This asymmetry simply results from that the decrease of

MBH spins during the period of consecutive TDS accretion is more rapid than the increase of MBH spins during the AGN period when those spins are large. One should also note that the occurrence of retrograde accretion is almost the same as prograde one in the TDS accretion episodes, while the fraction of retrograde-spin one in the gas-cloud accretion (AGN) episodes is negligible.

By comparing our model results on the spin distribution with the observational measurements of MBH spins via Fe K $\alpha$  line for a number of individual AGNs with mass  $\sim 10^6 M_\odot$ , we find that the contribution to MBH growth from accreting TDSs is insignificant ( $\lesssim 10\%$ ). However, the constraint on spins obtained from the stacked X-ray spectra of a larger number of NLS1s (Liu et al. 2015) suggests the contribution of TDS accretion to the growth of MBHs with mass  $\sim 10^6 M_\odot$  may be significant ( $\gtrsim 50\%$ ), which is in contradiction with the constraint inferred from the individual spin measurements. A large unbiased sample of spin measurements for AGNs is required in order to put a strong constraint on the contribution of accretion of TDSs to the growth of MBHs with mass  $\sim 10^6 M_\odot$ .

Current observations of TDEs are still not able to put constraints on the spins of their central MBHs. However, it is expected that future observations can provide strong constraints on the MBH spins through spin-induced Lense-Thirring precession (Stone & Loeb 2012), Quasi-Periodic Oscillations (QPOs) (Reis et al. 2012; Pasham et al. 2019), or other signatures. With QPO measurement in ASASSB-14li, a TDE with cen-

tral MBH mass  $\sim 10^{5.8-7.1} M_\odot$ , Pasham et al. (2019) recently found that the spin of this MBH should be greater than 0.7. This high spin in the TDS accretion state may also suggest that the contribution of TDS accretion to MBH growth is not significant (see Fig. 2), similar to that by the Fe K $\alpha$  line measurements of spins for other  $\sim 10^6 M_\odot$  MBHs in the AGN states (see Table 1).

We anticipate that future measurements on the spins of some  $\sim 10^6 M_\odot$  MBHs and determination of their spin distribution in both the gas-cloud (AGN) and the TDS accretion episodes will put strong constraints on the significance of the accretion of TDSs to the growth history of those MBHs. In addition, the comparison of the two spin distributions would put further constraints. For example, the accretion of TDSs to the growth of  $\sim 10^6 M_\odot$  MBHs would be important if the fraction of highly spinning MBHs in the TDS accretion episodes is found to be relatively small comparing to that in the gas-cloud (AGN) accretion episodes.

We thank Qingjuan Yu for helpful discussions on and contributions to various aspects presented in this paper. This work is partly supported by the National Key Program for Science and Technology Research and Development (Grant No. 2016YFA0400704), the National Natural Science Foundation of China (Grant No. 11873056, 11690024, and 11390372), and the Strategic Priority Program of the Chinese Academy of Sciences (Grant No. XDB 23040100).

## REFERENCES

- Artymowicz, P., Lin, D. N. C., & Wampller, E. J. 1993, *ApJ*, 409, 592
- Bardeen, J. M., & Petterson, J. A. 1975, *ApJ*, 195, 65
- Barausse, E. 2012, *MNRAS*, 423, 2533
- Bardeen, J. M., Press, W. H., & Teukolsky, S. A. 1972, *ApJ*, 178, 347
- Beloborodov, A. M., Illarionov, A. F., Ivanov, P. B., & Polnarev, A. G. 1992, *MNRAS*, 259, 209
- Berti, E., Volonteri, M. 2008, *ApJ*, 684, 822
- Blanchard, P. K., Nichols, M., Berger, E., et al. 2017, *ApJ*, 843, 106
- Brenneman, L. 2013, *AcPol*, 53, 652
- Brenneman, L. W., & Reynolds, C. S. 2006, *ApJ*, 652, 1028
- Capellupo, D. M., Netzer, H., Lira, P., Trakhtenbrot, B., & Mejía-Restrepo, J. 2016, *MNRAS*, 460, 212
- Cui, X., & Yu, Q. 2014, *MNRAS*, 437, 777
- de Felice, F. 1980, *Journal of Physics A Mathematical General*, 13, 1701
- Done, C., & Jin, C. 2016, *MNRAS*, 460, 1716
- Donley, J. L., Brandt, W. N., Eracleous, M., Boller, Th. 2002, *AJ*, 124, 1308
- Dotti, M., Colpi, M., Pallini, S., et al. 2013, *ApJ*, 762, 68
- Esquej, P., Saxton, R. D., Komossa, S., et al. 2008, *A&A*, 489, 543
- Figer, D. F., Kim, S. S. Morris, M., et al. 1999, *ApJ*, 525, 750
- Foucart, F., & Lai, D. 2014, *MNRAS*, 445, 1731
- Franchini, A., Lodato, G., & Facchini, S. 2016, *MNRAS*, 455, 1946
- Frolov, V. P., & Novikov, I. D. 1998, *Black hole physics : basic concepts and new developments /by Valeri P. Frolov and Igor D. Novikov. Dordrecht : Kluwer Academic, c1998. (Complete rewriting of The Physics of Black Holes, 1989, Kluwer.)*
- Gezari, S., Basa, S., Martin, D. C. 2008, *ApJ*, 676, 944
- Goodman, J. 2003, *MNRAS*, 339, 937
- Habibi, M., Stolte, A., Brandner, W., et al. *A&A*, 2013, 556, 26
- Harfst, S., Portegies, Zwart, S., & Stolte, A. 2010, *MNRAS*, 409, 628
- Herrnstein, J. R., Moran, J. M., et al. 1998, *ApJ*, 497, 69
- Herrnstein, J. R., Moran, J. M., Greenhill, L. J. & Trotter, A. S. 2005, *ApJ*, 629, 719
- Heyer, M., & Dame, T. M. 2015, *ARA&A*, 53, 583
- Hills, J. G. 1975, *Nature*, 254, 295
- Hughes, S. A. 2000, *Phys. Rev. D*, 61, 084004
- Hughes, S. A. 2001, *Phys. Rev. D*, 64, 064004
- Ishhara, Y., & Nakai, N. 2002, *IAUS*, 206, 400
- Kerr, R. P. 1963, *Physical Review Letters*, 11, 237
- Kesden, M. 2012, *Phys. Rev. D*, 85, 024037
- King, A. R., Lubow, S. H., Ogilvie, G. I., & Pringle, J. E. 2005, *MNRAS*, 363, 49
- King, A. R., & Pringle, J. E. 2006, *MNRAS*, 373, L90
- King, A. R., & Pringle, J. E. 2007, *MNRAS*, 377, L25
- King, A. R., Pringle, J. E., & Hofmann, J. A. 2008, *MNRAS*, 385, 1621
- Kolykhalov, P. I., & Sunyaev, R. A. 1980, *SvAL*, 6, 357
- Komossa, S. 2015, *Journal of High Energy Astrophysics*, 7, 148
- Kormendy, J., & Ho, L. C. 2013, *ARA&A*, 51, 511
- Milosavljević, M., Merritt, D., & Ho, L. C. 2006, *ApJ*, 652, 120
- Lense, J., & Thirring, H. 1918, *Physikalische Zeitschrift*, 19,
- Levin, Y., & Beloborodov, A. M. 2003, *ApJ*, 590, L33
- Liu, Z., Yuan, W., Lu, Y., & Zhou, X. 2015, *MNRAS*, 447, 517
- Lodato, G., & Rossi, E. M. 2011, *MNRAS*, 410, 359
- Lu, J. R., Ghez, A. M., Hornstein, S. D., et al. 2009, *ApJ*, 690, 1463
- Magorrian, J., & Tremaine, S. 1999, *MNRAS*, 309, 447
- Marconi, A., Risaliti, G., Gilli, R., et al. 2004, *MNRAS*, 351, 169
- Martin, R. G., Pringle, J. E., & Tout, C. A. 2007, *MNRAS*, 381, 1617
- McHardy, I. M., Gunn, K. F., Uttley, P., & Goad, M. R. 2005, *MNRAS*, 359, 1469
- Menezes, R. B., da Silva, P., & Steiner, J. E. 2018, *MNRAS*, 473, 2198
- Miralda-Escudé, J., & Kollmeier, J. A. 2005, *ApJ*, 619, 30
- Nayakshin, S., & Cuadra, J. 2005, *A&A*, 437, 437
- Nelson, R. P., & Papaloizou, J. C. B. 1999, *MNRAS*, 309, 929
- Nixon, C., & King, A. 2016, *LNP*, 905, 45
- Novikov, I. D., & Thorne, K. S. 1973, *Black Holes (Les Astres Occlus)*, 343

- Pasham, D. R., Remillard, R. A., Fragile, P. C., et al. 2019, *Science*, 363, 531
- Patrick, A. R., Reeves, J. N., Porquet, D., et al. 2012, *MNRAS*, 426, 2522
- Paumard, T., Genzel, R., Martins, F., et al. 2006, *ApJ*, 643, 1011
- Perego, A., Dotti, M., Colpi, M., & Volonteri, M. 2009, *MNRAS*, 399, 2249
- Peterson, B. M., Ferrarese, L., Gilbert, K. M., et al. 2004, *ApJ*, 613, 682
- Rees, M. J. 1988, *Nature*, 333, 523
- Reis, R. C., Miller, J. M., Reynolds, M. T., et al. 2012, *Science*, 337, 949
- Reynolds, C. S. 2014, *SSRv*, 183, 277
- Risaliti, G., Harrison, F. A., Madsen, K. K., et al. 2013, *Nature*, 494, 449
- Risaliti, G., Miniutti, G., Elvis, M., et al. 2009, *ApJ*, 696, 160
- Sądowski, A., Bursa, M., Abramowicz, M., et al. 2011, *A&A*, 532, A41
- Shakura, N. I., & Sunyaev, R. A. 1973, *A&A*, 24, 337
- Shankar, F., Weinberg, D. H., & Miralda-Escudé, J. 2009, *ApJ*, 690, 20
- Sesana, A., Barausse, E., Dotti, M., Rossi, E. M. 2014, *ApJ*, 794, 104
- Sołtan, A. 1982, *MNRAS*, 200, 115
- Stone, N., & Loeb, A. 2012, *Phys. Rev. Lett.*, 108, 061302
- Stone, N., Loeb, A., & Berger, E. 2013, *Phys. Rev. D*, 87, 084053
- Stone, N. C., & Metzger, B. D., 2016, *MNRAS*, 455, 859
- Strubbe, L. E., & Quataert, E. 2009, *MNRAS*, 400, 2070
- Thorne, K. S. 1974, *ApJ*, 191, 507
- Trakhtenbrot, B. 2014, *ApJ*, 789, L9
- van Valzen, S., & Farrar, G. R. 2014, *ApJ*, 792, 53
- Vasiliev, E., Antonini, F., & Merritt, D. 2015, *ApJ*, 810, 49
- Vasudevan, R. V., Fabian, A. C., Reynolds, C. S., et al. 2016, *MNRAS*, 458, 2012
- Volonteri, M., Madau, P., Quataert, E., & Rees, M. J. 2005, *ApJ*, 620, 69
- Volonteri, M., Sikora, M., & Lasota, J.-P. 2007, *ApJ*, 667, 704
- Volonteri, M., Sikora, M., Lasota, J.-P., & Merloni, A. 2013, *ApJ*, 775, 94
- Walton, D. J., Nardini, E., Fabian, A. C., Gallo, L. C., & Reis, R. C. 2013, *MNRAS*, 428, 2901
- Wang, J., & Merritt, D. 2004, *ApJ*, 600, 149
- Yamauchi, A., Nakai, N., Ishihara, Y., Diamond, P. & Sato, N. 2012, *PASJ*, 64, 103
- Yu, Q., & Tremaine, S. 2002, *MNRAS*, 335, 965
- Yu, Q., & Lu, Y. 2004, *ApJ*, 602, 603
- Yu, Q., & Lu, Y. 2008, *ApJ*, 689, 732
- Zhang, X., & Lu, Y. 2019, *ApJ*, 873, 101
- Zhou, X.-L., & Wang, J.-M. 2005, *ApJ*, 618, L83
- Zoghbi, A., Fabian, A. C., Uttley, P., et al. 2010, *MNRAS*, 401, 2419